Spring 5-1-2023

Deformation at Uturuncu Volcano, Bolivia: Modeling the Effect of Volatile Movement in the Hydrothermal System

Karissa Rosenberger
University of New Mexico

Karissa Rosenberger

Candidate

Earth and Planetary Sciences

Department

This thesis is approved, and it is acceptable in quality and form for publication

Approved by the Thesis Committee:

Tobias Fischer, Chairperson

Eric Lindsey

Brandon Schmandt

Patricia Nadeau

DEFORMATION AT UTURUNCU VOLCANO, BOLIVIA: MODELING THE EFFECT OF VOLATILE MOVEMENT IN THE HYDROTHERMAL SYSTEM

by

KARISSA ROSENBERGER

B.S. EARTH SCIENCE, NEW MEXICO INSTITUTE OF MINING AND TECHNOLOGY, 2020

THESIS

Submitted in Partial Fulfillment of the

Requirements for the Degree of

Master of Science

Earth and Planetary Sciences

The University of New Mexico

Albuquerque, New Mexico

May, 2023

Acknowledgements

I want to thank everyone who has supported and encouraged me during the pursuit of my Master's degree. I want to especially thank my advisor, Tobias Fischer, for his advice and guidance throughout the entire process. He was always available to questions and discussions and constantly tried to help me think through the problem and come to my own conclusions. I have learned an immense amount about volcanology, gas geochemistry, and generally how to conduct scientific research under Tobias's guidance.

I also want to thank Eric Lindsey for his help with Python and answering my numerous questions about bugs and issues with my code. With his help, I became a much better programmer and that knowledge will be incredibly valuable as I move on to the next thing. Additionally, I want to thank Tricia Nadeau for her support and guidance during my summer at Kīlauea and beyond.

My friends have been an invaluable part of this process, providing support, encouragement, and distraction from the research when it was especially challenging. I want to particularly thank Jordan for the conversations, laughs, and adventures over the past couple years even though we live several states apart. Additional thanks go to Ian and my brother, Will, for helping me understand technology and figure out the ever confusing world of programming.

Finally, a deep thank you to my parents who have always believed in me and encouraged me to go for my dreams, no matter how large or challenging. I would not be where I am today without their continual love and support.

Deformation at Uturuncu Volcano, Bolivia: Modeling the Effect of Volatile Movement in the Hydrothermal System

by

Karissa Rosenberger

B.S., Earth Science, New Mexico Institute of Mining and Technology, 2020

M.S., Earth and Planetary Sciences, University of New Mexico, 2023

Abstract

Deformation at volcanos is often a precursor to an eruption, but sometimes volcanos experience uplift without actually erupting. Determining the mechanisms behind this deformation and whether it will lead to an eruption is an important part of understanding volcanic systems. Uturuncu volcano in Bolivia has been experiencing deformation for decades, but the last time it erupted was 250,000 years ago. The reason behind this deformation is unknown, but one possible cause is volatiles moving into the hydrothermal system and getting trapped, causing the volume to increase and the surface to uplift. To test this hypothesis, the current volume change of Uturuncu's hydrothermal system was calculated using Interferometric Synthetic Aperature Radar (InSAR) data from the region. TOUGH3, a numerical modeling software, was then used to determine the volume change of the system with varying inputs of CO_2 and H_2O. With this information, it was determined that CO_2 injection could potentially cause the recent uplift of 2-3 mm/yr at Uturuncu. However, a few decades ago, Uturuncu was uplifting at a rate

of 1 cm/yr and modeling shows that there is not enough gas in the system to support injecting sufficient CO_2 to cause this level of surface deformation. Thus, something else was likely causing this 1 cm/yr uplift, such as magma injection.

There are a wide range of volatiles that are useful for understanding volcanic systems and predicting behavior. The properties of helium make it an excellent geochemical tracer and further study into this gas can aid in understanding the processes occurring at depth in volcanic environments. A method for directly calculating helium flux was tested at the Sulphur Springs geothermal system located in the Valles Caldera in New Mexico (NM) and this method can be implemented at many volcanic systems worldwide. Fick's Law was used to calculate a diffusive helium flux of 0.068-0.187 tons/year. These results were validated using the calculated helium flux and the CO_2/He ratio to determine the CO_2 flux which was then compared to previous CO_2 flux surveys conducted at Sulphur Springs. The Sulphur Springs helium flux was then compared to other volcanic systems, such as volcanos in the Canary Islands, Yellowstone Caldera, and Wakamiko Caldera in Japan in order to understand how the Sulphur Springs system compares with other regions. Overall, the maximum helium flux of 0.187 tons/year falls towards the lower end of the measured volcanic helium fluxes.

The final volcanic system investigated was Kīlauea in Hawaii. During the summer of 2021, an extensive CO_2 survey of the Kīlauea caldera and rim was carried out with the goal of identifying and mapping high CO_2 emission areas. Two MultiGAS instruments mounted on backpack frames were used to measure CO_2, SO_2, and H_2S concentrations anywhere in and around the caldera that could be safely traversed on foot. The resulting

data was interpolated using simple kriging in the ArcGIS Geostatistical Analyst extension in order to produce a map of CO_2 concentrations across the entire caldera. This map was compared to two previous CO_2 surveys that covered smaller areas of the caldera. From these comparisons, it was determined that there has not been much change in the CO_2 degassing pathways over the past 20 years despite the massive 2018 caldera eruption and collapse. Finally, two potential methods for measuring the total CO_2 flux from Kīlauea were discussed. Both methods require further research and testing in order to determine if they are plausible approaches for calculating the CO_2 emission rate from Kīlauea.

Table of Contents

List of Figures

List of Tables

Chapter 1: Introduction

Volcanoes can be incredibly devastating because of the destruction and unpredictability associated with eruptions. Understanding the underlying mechanisms and factors influencing volcanic unrest is vital for potentially predicting future eruptions or activity. One primary factor that is often monitored is uplift or subsidence at volcanos. This deformation is generally attributed to magma movement and can be a precursor to an impending eruption (Sparks, 2003; Brenguier et al., 2008; Rouwet et al., 2014). However, deformation is not always followed by an eruption, so understanding other potential causes is important for correctly interpreting unrest at a volcano. This thesis focuses on volatiles at Uturuncu Volcano in Bolivia and how volatile movement in the hydrothermal system influences the observed deformation. Methods to measure and investigate volatiles in two other volcanic systems (Sulphur Springs geothermal system in New Mexico (NM) and Kīlauea in Hawaii) are also examined.

Uturuncu is a Pleistocene dacitic volcano in southern Bolivia that last erupted 250 thousand years ago (Pritchard et al., 2018). Despite the time since its last eruption, Uturuncu is still actively degassing and deforming. For the past several decades, Uturuncu has been experiencing varying rates of uplift around the summit and this uplifting area is surrounded by a circular region of subsidence (Fialko and Pearse, 2012; Henderson and Pritchard, 2013, 2017; Lau et al., 2018). The reason for this uplift is unknown, but some argue that magma and material rising from the Altiplano-Puna Magma Body (APMB) could result in the observed deformation (Sparks et al., 2008; Fialko and Pearse, 2012). However, another

potential explanation for the deformation is volatiles moving into Uturuncu's hydrothermal system and getting trapped there, which would increase the pressure and result in uplift. The purpose of this project was to test this hypothesis and determine the plausibility of volatile movement causing the observed uplift.

The first step was determining how much the hydrothermal system is expanding based on the uplift rate. Interferometric Synthetic Aperture Radar (InSAR) data from the region was used to calculate the volume change at the surface (Fialko and Pearse, 2012; Henderson and Pritchard, 2017; Lau et al., 2018), which was then assumed to be the same as the volume change at the depth of the hydrothermal system. These calculations give how much the volume of the hydrothermal system is changing based on the uplift rate reflected in the InSAR data. Two different time ranges were used for these calculations: 1992-2011 (Fialko and Pearse, 2012; Henderson and Pritchard, 2017) and 2014-2017 (Lau et al., 2018). These time ranges mark the approximate time when the uplift rate at Uturuncu decreased from ~1 cm/yr to 2-3 mm/yr (Pritchard et al., 2018).

TOUGH3 is a numerical modeling software that was used to simulate injection of CO_2 and H_2O into a cylindrical model of Uturuncu's hydrothermal system (Jung et al., 2018). Varying amounts of these volatiles were injected at the base of the model and CO_2 and H_2O were degassed at a fixed rate from the surface. The model output was the volume change of the system after volatile injection. Comparing the modeled volume change to the actual volume change calculated from the InSAR data allows determination of the CO_2 injection required to cause the observed deformation. These CO_2 injection rates were compared to actual amounts of CO_2 degassed from other volcanos around the world in order to determine

how realistic the CO_2 injections rates are for Uturuncu. Based on this information, determinations about whether Uturuncu's deformation could be caused purely by volatile movement or if something else, such as magma injection, was required to cause the uplift could be made.

Understanding the potential reasons behind Uturuncu's deformation and whether volatile movement contributes to the uplift could potentially impact how scientists view and interpret other volcanos. In general, knowledge of volatile movement and volatile fluxes from volcanic systems can be vital for drawing conclusions about current and future volcanic activity. Two other volcanic systems are explored in this thesis: the Sulphur Springs geothermal system in Valles Caldera, NM and Kīlauea in Hawaii. Continually expanding knowledge of volatiles in different volcanic systems will lead to better understandings of subsurface volatile movements and potential volcanic activity.

While CO_2 is one of the primary gases emitted from volcanos, helium is also degassed and is an excellent geochemical tracer that can help with understanding processes occurring in volcanic systems (Padrón et al., 2012). Helium flux can be used in a variety of ways, including as a precursor to volcanic unrest (Padrón et al., 2013), locating potential geothermal resources (Rodríguez et al., 2015; Alonso et al., 2022), tracing degassing of magmatic bodies (Boucher et al., 2018; Alonso et al., 2021), and calculating other volatile fluxes (Hilton et al., 2002). Sulphur Springs is a geothermal system in the Valles Caldera, NM that has been previously investigated as a potential source of geothermal energy (Goldstein et al., 1982; Goff et al., 1992; Trainer et al., 2000). CO_2 surveys have been carried out in this system, but not much is known about the helium degassing and helium flux. This

project focused on collecting soil gas samples from Sulphur Springs and then using that data and Fick's Law to determine the diffusive helium flux for the area. This is a method that is widely applicable and can be used in other volcanic systems.

Kīlauea is a highly studied volcano because of its regular, non-violent eruptions (Tilling and Dvorak, 1993). Small scale CO_2 concentration surveys have been carried out in the past at Kīlauea, but they only covered small portions of the caldera. One goal of this project was to conduct an extensive CO_2 survey of the caldera and rim in order to make a comprehensive map detailing the areas with the highest CO_2 concentrations. This map is a first step towards generating an estimate of the total CO_2 flux from Kīlauea. Measuring the CO_2 flux from Kīlauea has been a difficult challenge since the appearance of the 2008 summit lava lake. This is an ongoing issue and some potential ideas to measure the CO_2 flux are discussed.

Overall, this thesis investigates volatiles in three different volcanic systems: Uturuncu Volcano in Bolivia, Sulphur Springs geothermal area in NM, and Kīlauea in Hawaii. Specifically, the possible connection between volatile movement and deformation is explored at Uturuncu in order to understand why a Pleistocene age volcano is currently exhibiting signs of unrest. Different methods for studying helium and CO_2 were tested at the other two volcanic systems. All of these methods can be applied to other volcanic systems around the world in order to better understand and characterize them.

References

Alonso, M. et al., 2021, Changes in the thermal energy and the diffuse 3He and 4He degassing prior to the 2014–2015 eruption of Pico do Fogo volcano, Cape Verde: Journal of Volcanology and Geothermal Research, v. 416, p. 107271, doi:10.1016/j.jvolgeores.2021.107271.

Alonso, M. et al., 2022, Thermal energy and diffuse 4He and 3He degassing released in volcanic-geothermal systems: Renewable Energy, v. 182, p. 17–31, doi:10.1016/j.renene.2021.10.016.

Boucher, C., Lan, T., Marty, B., Burnard, P.G., Fischer, T.P., Ayalew, D., Mabry, J., Maarten de Moor, J., Zelenski, M.E., and Zimmermann, L., 2018, Atmospheric helium isotope composition as a tracer of volcanic emissions: A case study of Erta Ale volcano, Ethiopia: Chemical Geology, v. 480, p. 3–11, doi:10.1016/j.chemgeo.2017.05.011.

Brenguier, F., Shapiro, N.M., Campillo, M., Ferrazzini, V., Duputel, Z., Coutant, O., and Nercessian, A., 2008, Towards forecasting volcanic eruptions using seismic noise: Nature Geoscience, v. 1, p. 126–130, doi:10.1038/ngeo104.

Fialko, Y., and Pearse, J., 2012, Sombrero Uplift Above the Altiplano-Puna Magma Body: Evidence of a Ballooning Mid-Crustal Diapir: Science, v. 338, p. 250–252, doi:10.1126/science.1226358.

Goff, F., Gardner, J.N., Hulen, J.B., Nielson, D.L., Charles, R., WoldeGabriel, G., Vuataz, F.-D., Musgrave, J.A., Shevenell, L., and Kennedy, B.M., 1992, The Valles caldera hydrothermal system, past and present, New Mexico, USA: Scientific Drilling, v. 3, p. 181–204.

Goldstein, N.E., Holman, W.R., and Molloy, M.W., 1982, Final report of the Department of Energy Reservoir Definition Review Team for the Baca Geothermal Demonstration Project: Lawrence Berkeley Lab., CA (USA) LBL-14132, doi:10.2172/6764368.

Henderson, S.T., and Pritchard, M.E., 2013, Decadal volcanic deformation in the Central Andes Volcanic Zone revealed by InSAR time series: Geochemistry, Geophysics, Geosystems, v. 14, p. 1358–1374, doi:https://doi.org/10.1002/ggge.20074.

Henderson, S.T., and Pritchard, M.E., 2017, Time-dependent deformation of Uturuncu volcano, Bolivia, constrained by GPS and InSAR measurements and implications for source models: Geosphere, v. 13, p. 1834–1854, doi:10.1130/GES01203.1.

Hilton, D., Fischer, T., and Marty, B., 2002, Noble Gases and Volatile Recycling at Subduction Zones: Reviews in Mineralogy & Geochemistry - REV MINERAL GEOCHEM, v. 47, p. 319–370, doi:10.2138/rmg.2002.47.9.

Jung, Y., Pau, G.S.H., Finsterle, S., and Doughty, C., 2018, TOUGH3 User's Guide:

Lau, N., Tymofyeyeva, E., and Fialko, Y., 2018, Variations in the long-term uplift rate due to the Altiplano–Puna magma body observed with Sentinel-1 interferometry: Earth and Planetary Science Letters, v. 491, p. 43–47, doi:10.1016/j.epsl.2018.03.026.

Padrón, E. et al., 2013, Diffusive helium emissions as a precursory sign of volcanic unrest: Geology, v. 41, p. 539–542, doi:10.1130/G34027.1.

Padrón, E., Pérez, N.M., Hernández, P.A., Sumino, H., Melián, G., Barrancos, J., Nolasco, D., and Padilla, G., 2012, Helium emission at Cumbre Vieja volcano, La Palma, Canary Islands: Chemical Geology, v. 312–313, p. 138–147, doi:10.1016/j.chemgeo.2012.04.018.

Pritchard, M.E. et al., 2018, Synthesis: PLUTONS: Investigating the relationship between pluton growth and volcanism in the Central Andes: Geosphere, v. 14, p. 954–982, doi:10.1130/GES01578.1.

Rodríguez, F. et al., 2015, Diffuse Helium and Hydrogen Degassing to Reveal Hidden Geothermal Resources in Oceanic Volcanic Islands: The Canarian Archipelago Case Study: Surveys in Geophysics, v. 36, p. 351–369, doi:10.1007/s10712-015-9320-8.

Rouwet, D., Sandri, L., Marzocchi, W., Gottsmann, J., Selva, J., Tonini, R., and Papale, P., 2014, Recognizing and tracking volcanic hazards related to non-magmatic unrest: a review: Journal of Applied Volcanology, v. 3, p. 17, doi:10.1186/s13617-014-0017-3.

Sparks, R.S.J., 2003, Forecasting volcanic eruptions: Earth and Planetary Science Letters, v. 210, p. 1–15, doi:10.1016/S0012-821X(03)00124-9.

Sparks, R.S.J., Folkes, C.B., Humphreys, M.C.S., Barfod, D.N., Clavero, J., Sunagua, M.C., McNutt, S.R., and Pritchard, M.E., 2008, Uturuncu volcano, Bolivia: Volcanic unrest due to mid-crustal magma intrusion: American Journal of Science, v. 308, p. 727–769, doi:10.2475/06.2008.01.

Tilling, R.I., and Dvorak, J.J., 1993, Anatomy of a basaltic volcano: Nature, v. 363, p. 125–133, doi:10.1038/363125a0.

Trainer, F.W., Rogers, R.J., and Sorey, M.L., 2000, Geothermal hydrology of Valles caldera and the southwestern Jemez Mountains: U.S Geological Survey Water-Resources Investigations Report 00–4067.

Chapter 2: Volatile movement in the hydrothermal system of Uturuncu, Bolivia

2.1 Introduction

2.1.1 Deformation mechanisms and volatile movement in volcanic systems

Typically, deformation at a volcano is attributed to the movement of magma beneath Earth's crust. As magma rises through conduits and cracks in the ground, pressure builds and leads to the surrounding rocks deforming and uplifting at Earth's surface, a phenomenon that can be measured using various techniques (Sparks, 2003). Surface uplift as well as increased seismicity and gas emission are often indicative of an impending volcanic eruption or other volcanic hazard (Sparks, 2003; Brenguier et al., 2008; Rouwet et al., 2014). A famous example of surface deformation preceding a period of violent volcanic activity was the eruption of Mount St. Helens in 1980 (Cashman and Hoblitt, 2004). While the occurrence of these precursors does not always mean an imminent eruption, it is important to monitor them in order to understand how processes occurring beneath the surface may influence volcanic activity (Sparks, 2003; Rouwet et al., 2014).

Rising magma releases volatiles and the volatile content is typically dominated by H_2O and CO_2 with generally smaller amounts of S, Cl, and F (de Vivo et al., 2005; Fischer and Chiodini, 2015). While volatiles typically constitute only a few weight percent of a magma, they are a major driver behind volcanic eruptions (Edmonds and Wallace, 2017). As pressure decreases, the solubility of volatiles in magma also decreases which makes

degassing more likely as magma rises (de Vivo et al., 2005). Additionally, gases will expand significantly as the pressure decreases (de Vivo et al., 2005). Of the volatile species typically emitted, CO_2 has the lowest solubility so it enters the vapor phase first, generally followed by H_2O (Fischer and Chiodini, 2015). After CO_2 and H_2O have exsolved, other less abundant volatile species join them in the vapor phase (Fischer and Chiodini, 2015).

Another possible explanation for the exsolution of volatiles out of magma occurs during the cooling and crystallization of magma. Low-volatile or volatile-free minerals will preferentially crystallize first, causing an accumulation of volatiles in the remaining melt (de Vivo et al., 2005). Over time, the increasing concentration of volatiles will reach the saturation point for that specific temperature, pressure, and composition and the volatiles will begin to exsolve (de Vivo et al., 2005). Once at the surface, the volatiles typically degas through high-temperature crater fumaroles, fumaroles formed by boiling water in aquifers, or by passive degassing through the soil (Fischer and Chiodini, 2015).

The Uturuncu volcano in southern Bolivia has been experiencing deformation for decades. Satellite data indicates that the region surrounding the volcano has been uplifting at a rate of approximately 1 cm/yr since the early 1990s, although this has slowed down in recent years (Fialko and Pearse, 2012; Henderson and Pritchard, 2013, 2017; Lau et al., 2018). Many attribute this uplift to magma rising from the underlying Altiplano Puna magma body (APMB) towards the surface (Sparks et al., 2008; Fialko and Pearse, 2012). However, as volatiles exsolve and rise towards the surface they may get trapped in the hydrothermal system instead of immediately degassing at Uturuncu's summit. This would cause a buildup of pressure in the hydrothermal system which could impact the deformation observed at the

surface. In this discussion, the potential connection between volatile movement in Uturuncu's hydrothermal system and the observed deformation was investigated.

2.1.2 Uturuncu volcano, Bolivia

Along the western coast of South America runs the Andes, a mountain range created by the subduction of the Nazca plate beneath the South American plate. While subduction has been occurring in this region since the Mesozoic era (251-65.5 Ma), it was not until the Miocene (~26 Ma) when the Farallon plate broke up into the Nazca and Cocos plates that the uplift of the Andes began in Bolivia (Sparks et al., 2008; Capitanio et al., 2011). This caused an increase in the convergence rate as well as a steepening of the angle of subduction, which led to the uplift of the Altiplano Plateau (Allmendinger et al., 1997; Sparks et al., 2008). The Altiplano Plateau is the second highest plateau in the world and overlies a region of thickened crust, largely caused by crustal shortening as well as magmatic addition, lithospheric thinning, and other processes (Allmendinger et al., 1997).

Within the past 10 Ma, large ignimbrite eruptions in the Altiplano Plateau formed the Altiplano-Puna volcanic complex (APVC), covering an area of 50,000 km^2 (Silva, 1989; Sparks et al., 2008; Pritchard et al., 2018). Uturuncu volcano is located in southern Bolivia in the APVC (Figure 2.1) about 100 km behind the main volcanic arc (Sparks et al., 2008). Uturuncu is a Pleistocene dacitic volcano that last erupted 250 thousand years ago (Pritchard et al., 2018). This volcano is centrally located above an ultra-low velocity region that is interpreted to be a magma body found in the mid-crust known as the APMB (Chmielowski et al., 1999). Numerous approaches have been used to locate and examine the characteristics of

the APMB, including seismic, gravity, and electromagnetic methods (Chmielowski et al., 1999; Zandt et al., 2003a; Prezzi et al., 2009; Comeau et al., 2016). While Uturuncu is currently dormant, there are active fumarole fields at its summit that point to the still active magma body lying beneath it (Kukarina et al., 2017).

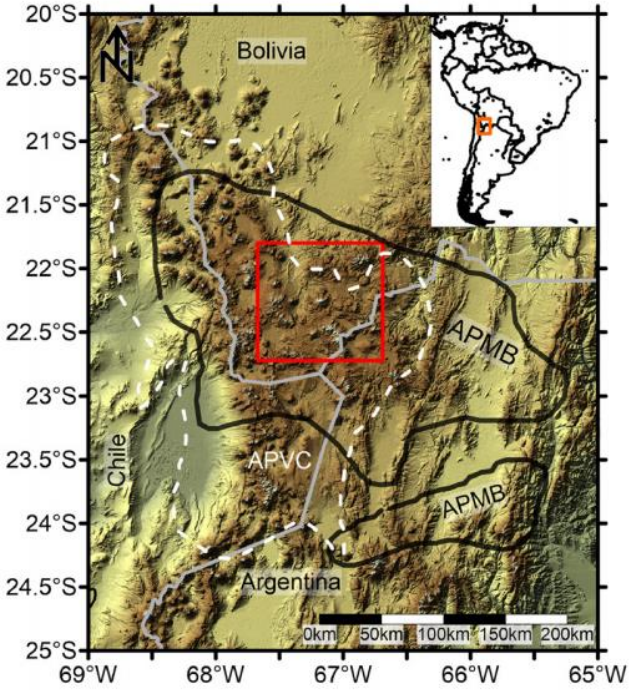

Figure 2.1: Location of Uturuncu volcano in southern Bolivia. Black line indicates the Altiplano-Puna magma body (APMB) and the white dashed line shows the extent of the Altiplano-Puna volcanic complex (APVC) (Kukarina et al., 2017).

A less studied aspect of Uturuncu is its hydrothermal system located at 2-4.5 km beneath the volcano (Pritchard et al., 2018; MacQueen et al., 2021). Its presence is indicated by various geophysical anomalies, such as low resistivity, low velocity, and earthquakes (Pritchard et al., 2018; MacQueen et al., 2021). During Uturuncu's eruptive periods, the magma was likely stored in a shallow magma chamber at approximately the same location of the current hydrothermal system (Pritchard et al., 2018). The presence of magma there today

would not explain the resistivity values, but they could be related to saline fluids and volatiles in the hydrothermal system (Comeau et al., 2016; Pritchard et al., 2018). The continued exsolution and trapping of volatiles in the hydrothermal system may increase the pressurization and result in the observed deformation.

2.1.3 Deformation history

Although Uturuncu has not erupted in recent history, it has been showing signs of unrest through uplift and subsidence around the volcanic center over the past several decades. Interferometric Synthetic Aperture Radar (InSAR) data has been used extensively to analyze the changing deformation from 1992 to present times (Fialko and Pearse, 2012; Henderson and Pritchard, 2013, 2017; Lau et al., 2018). Between 1992 and 2011, the uplift surrounding Uturuncu remained relatively constant at approximately 1 cm/year, although there is a suggestion that there may have been a slowdown in the deformation rate from 2003-2010 (Henderson and Pritchard, 2013, 2017). This region of uplift extends outwards from Uturuncu to about 40 km and is then surrounded by a ring of subsidence that extends out to 75 km (Figure 2.2) (Fialko and Pearse, 2012; Gottsmann et al., 2017). The ground is subsiding at a maximum rate of -4 mm/year, which is much slower than the uplift rate (Henderson and Pritchard, 2013).

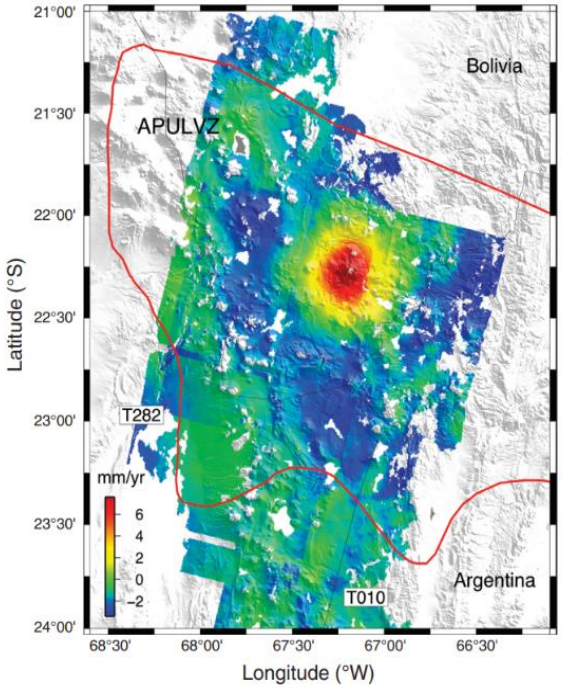

Figure 2.2: Uplift and subsidence surrounding Uturuncu. Red line indicates ultra-low velocity zone beneath Uturuncu (Fialko and Pearse, 2012).

More recent InSAR data shows that the uplift rate has decreased significantly surrounding Uturuncu (Henderson and Pritchard, 2017; Lau et al., 2018). Data from September, 2014 to December, 2017 collected by the Sentinel-1A/B satellites indicates a maximum uplift rate of 3-5 mm/year, compared to the ~1 cm/year from 1992-2011 (Lau et al., 2018). This data also revealed a localized zone to the south of Uturuncu that was subsiding at a rate of 9 mm/yr, possibly due to the collapse of a shallow hydrothermal system (Lau et al., 2018). These 3 years of data do not show the subsidence surrounding the uplift, likely because the subsidence is below the noise level detected by the satellites (Lau et al., 2018). Changing uplift and subsidence rates indicates the fluctuations over short time scales (e.g., months to years) of the deformation rate around Uturuncu (Lau et al., 2018).

2.1.4 Subsurface structure

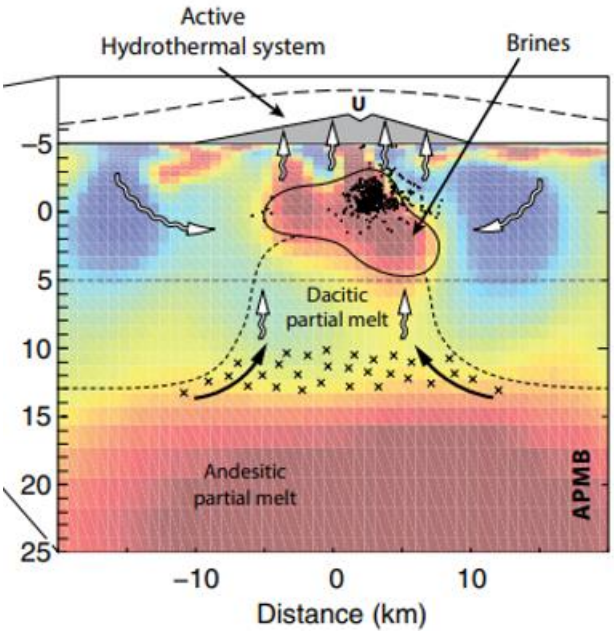

Figure 2.3: Subsurface structure beneath Uturuncu showing the Altiplano Puna Magma Body (ABMB) and the hydrothermal system. (Pritchard et al., 2018)

The subsurface structure of Uturuncu consists of a deep region of crustal melt known as the APMB that is connected to a shallow hydrothermal system (Figure 2.3). The APMB has been studied extensively using seismic, gravity, and electromagnetic methods (Chmielowski et al., 1999; Zandt et al., 2003b; Prezzi et al., 2009; Pritchard et al., 2018). It is approximately 200 km wide and 10-20 km thick at a depth of ~20 km (Pritchard et al., 2018). Much less is known about the hydrothermal system, but it is theorized to be at a depth of 2-4.5 km (Pritchard et al., 2018).

There are numerous models that speculate at the exact structure beneath Uturuncu and how it causes the volcano's deformation pattern. A common model proposes that there is a buoyant column or diapir rising from the APMB towards the surface beneath Uturuncu

(Fialko and Pearse, 2012; Gottsmann et al., 2017; Lau et al., 2018). Different models place varying levels of importance on whether it is primarily partial melts or primarily volatiles that are being transported towards the surface and causing the surface deformation (Fialko and Pearse, 2012; Gottsmann et al., 2017). Another model suggests that there is a magma source reservoir deflating in the lower crust while a sink reservoir is inflating in the middle crust (Henderson and Pritchard, 2017).

The overall goal of this project was to determine whether volatiles getting trapped in Uturuncu's hydrothermal system could contribute to the observed deformation at the volcano. First, InSAR data from the region was used to determine the volume change occurring due to the varying rates of uplift around the volcano. For this step, the assumption was made that the volume change at the surface would be similar to the volume change at the depth of the hydrothermal system. Then the flow of CO_2 and H_2O in the hydrothermal system was modeled using TOUGH3 (Jung et al., 2018). The output from this model was the volume change caused by injecting a specified amount of CO_2 and H_2O. By comparing these volume change calculations, the total amount of CO_2 injection required to cause the observed deformation is determined. These numbers are compared to the total amount of CO_2 typically degassed from volcanos around the world to how much CO_2 is actually available for degassing from the APMB in order to determine the validity of this hypothesis.

2.2 Methods

2.2.1 Volume change calculations

InSAR data from two different time periods at Uturuncu (1992-2011 and 2014-2017) was used to determine the volume change and to understand how it has changed between the higher deformation rates before 2011 and the lower deformation rates today. This method calculates the volume change at the surface and the assumption is made that the volume change at the depth of the hydrothermal system will be similar. Factors such as rock compressibility and the increased pressure at the depth of the hydrothermal system likely impacts the volume change, but for the purposes of this discussion, these factors were not considered.

Between 1992 and 2011, there was approximately 1 cm/yr of uplift occurring within a 40 km radius of Uturuncu's summit. Line of sight (LOS) data from Fialko and Pearse (2012) was used to calculate the volume change during this time period. This data includes both the outwards (radial) and upwards (vertical) components of deformation. Because the focus of this study was on uplift at Uturuncu, only the data located within 40 km of Uturuncu was used in the volume calculation. Any data outside of this circle was masked by setting it to zero. Additionally, there were occasional gaps in the data that were smoothed over using cubic interpolation. Python (version 3.10) was used to make these adjustments to the data (Figure 2.4). The area inside the circle was used to calculate the volume change including both the radial and vertical components.

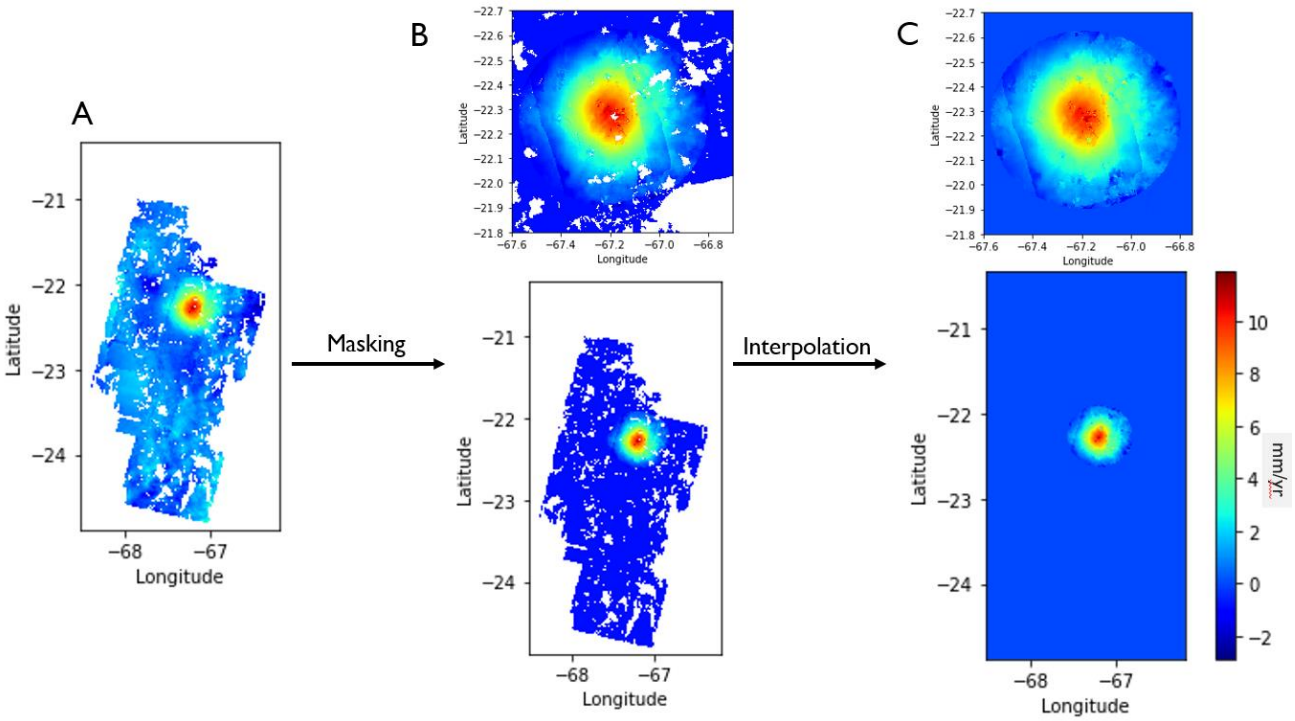

Figure 2.4: A) InSAR data from 1992-2011; B) For the volume change calculations, only the data within a 40 km radius of Uturuncu was of interest. All of the data outside of this circle was set to zero; C) The entire map was interpolated to remove gaps in the data.

The previous measurement was based only on the raw InSAR data. In Henderson and Pritchard (2017), the same dataset was decomposed into separate radial and vertical components (Figure 2.5), which allowed calculation of the volume change from 1992-2011 based only on the vertical deformation component. This was accomplished by calculating the area under the blue curve in Figure 2.5 using the trapezoidal rule and expanding it to three dimensions using the cylindrical coordinate system.

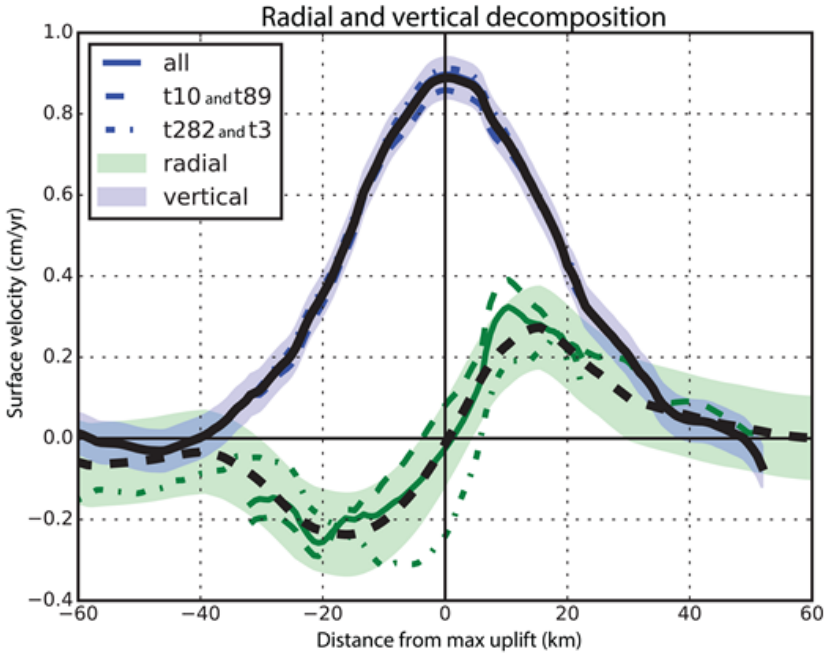

Figure 2.5: InSAR data from 1992-2011 decomposed into separate radial (green) and vertical (blue) components (Henderson & Pritchard, 2017).

After 2011, the deformation rate at Uturuncu dropped to 2-3 mm/yr and InSAR data from 2014-2017 reflects this change (Lau et al., 2018). This data consists of two ascending and two descending tracks (Figure 2.6), which need to be decomposed into the radial and vertical components to complete the volume change calculations.

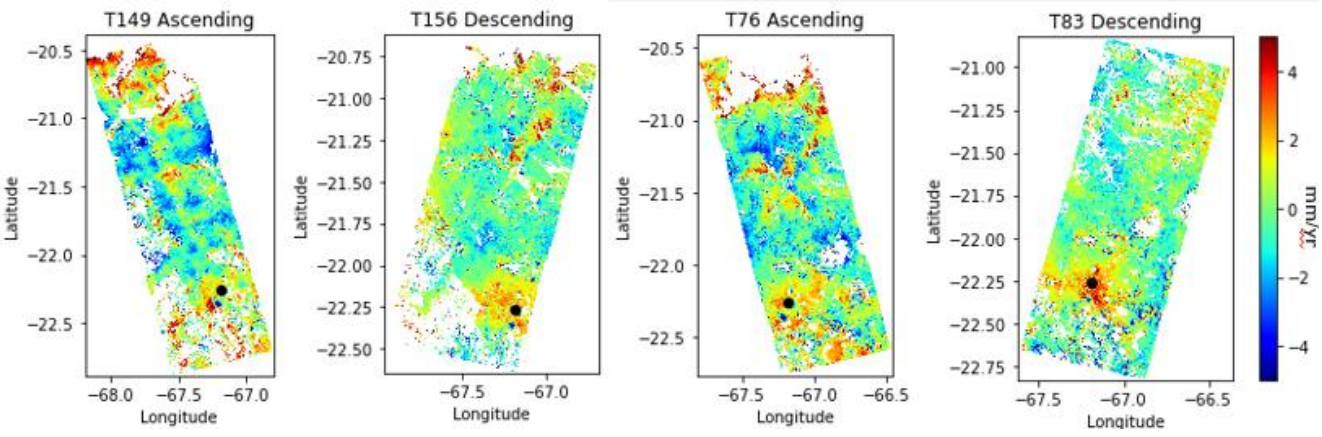

Figure 2.6: InSAR data from 2014-2017 showing the two ascending (T149 and T76) and two descending (T156 and T83) tracks. A black dot indicates Uturuncu's location.

In order to do this decomposition, a horizontal slice of data across Uturuncu was used to plot a profile of the deformation across the volcano. The slice needed to be relatively narrow, so that deformation in the N-S direction can be assumed to be zero. Equations 2.1 and 2.2 show the LOS directions for the ascending and descending tracks.

Equation 2.1: Ascending = +E – N + Up

Equation 2.2: Descending = -E – N + Up

Adding together the ascending and descending tracks, dividing by two, and then assuming N is zero results in the vertical deformation component. Subtracting the ascending and descending tracks and dividing by two gives the radial deformation component. The radial and vertical components were plotted and the area under the vertical deformation component was measured using the trapezoidal rule and extended to 3D using the cylindrical coordinate system. Different combinations of ascending and descending tracks produce differing values for the volume change.

2.2.2 VolatileCalc

VolatileCalc is a software that allows modeling of rhyolite H_2O-CO_2 isobaric solubility curves and open and closed system degassing paths for systems at magmatic temperatures and pressures (Newman and Lowenstern, 2002). This program was used to calculate the predicted H_2O/CO_2 molar ratio of the degassing magma based on an assumed H_2O wt% of 4.5 and the PT conditions of the magmatic system. PT conditions for deep degassing from the APMB and shallow degassing from Uturuncu's most recent eruption (250 ka) were found in Gottsmann et al., 2017. For the shallow degassing, the pressure was ~1270

bars and the temperature was ~876 °C. For the deep degassing, the pressure was 5400-6790 bars and the temperature was 975 °C. In VolatileCalc, the pressure only goes up to 5000 bars, so this was used as the pressure for the deep degassing scenario.

2.2.3 TOUGH3

TOUGH, or the Transport Of Unsaturated Groundwater and Heat, is a suite of software codes developed at the Lawrence Berkeley National Laboratory (LBNL) for modeling multi-phase, multi-component fluid and heat flow in fractured and porous media (Jung et al., 2018). Specifically, TOUGH3 combines previous serial and parallel implementations of the code as well as employing new and enhanced features, so this version of the TOUGH suite was chosen for this project. TOUGH3 has various equation of state (EOS) modules that allow modeling of different phases and components. EOS module ECO2N V2.0 was chosen for this project because it allows modeling of water, CO_2, and brine at high temperatures and pressures (Pan et al., 2015). This module can accommodate temperatures between 10-300 °C, pressures up to 600 bars, and allows the transition between gaseous and supercritical CO_2.

Previous models of Uturuncu's subsurface show a column structure with a radius of 6 km rising from the APMB towards the volcano and the depth of the hydrothermal system is estimated to be between 2 and 4.5 km (Gottsmann et al., 2017). These parameters were used to generate a mesh for the simulation with a depth of 4.5 km and a radius of 6 km (Figure 2.7). The depth was split into 50 m increments in order to allow analysis of fluid and gaseous flow from the bottom to the top. The top boundary of the mesh was set to fixed atmospheric

temperature and pressure conditions and the bottom boundary was set to fixed temperature and variable pressure, while the other boundaries were impermeable and adiabatic. Various rock properties including density, porosity, permeability, heat conductivity, and specific heat were set based on similar rock types in the Central Andes (Table 2.1). The gas output from the system was set to 40 kg H_2O/s and 20 kg CO_2/s. These values were calculated from data collected during an expedition to Uturuncu in 2018 (Fischer, unpublished). Sulphur is likely as significant volatile in this system, but is not considered in the model because TOUGH3 does not include sulphur.

Table 2.1: Rock properties used in the TOUGH3 model.

Density	2700 kg/m^3	Pritchard et al., 2018
Porosity	0.1	Sruoga et al., 2004
Permeability	$9.869x10^{-14}$ m^2	Sruoga et al., 2004
Heat conductivity	2.00 W/m/K	De Silva et al., 2006
Specific heat	980 J/kg/K	De Silva et al., 2006

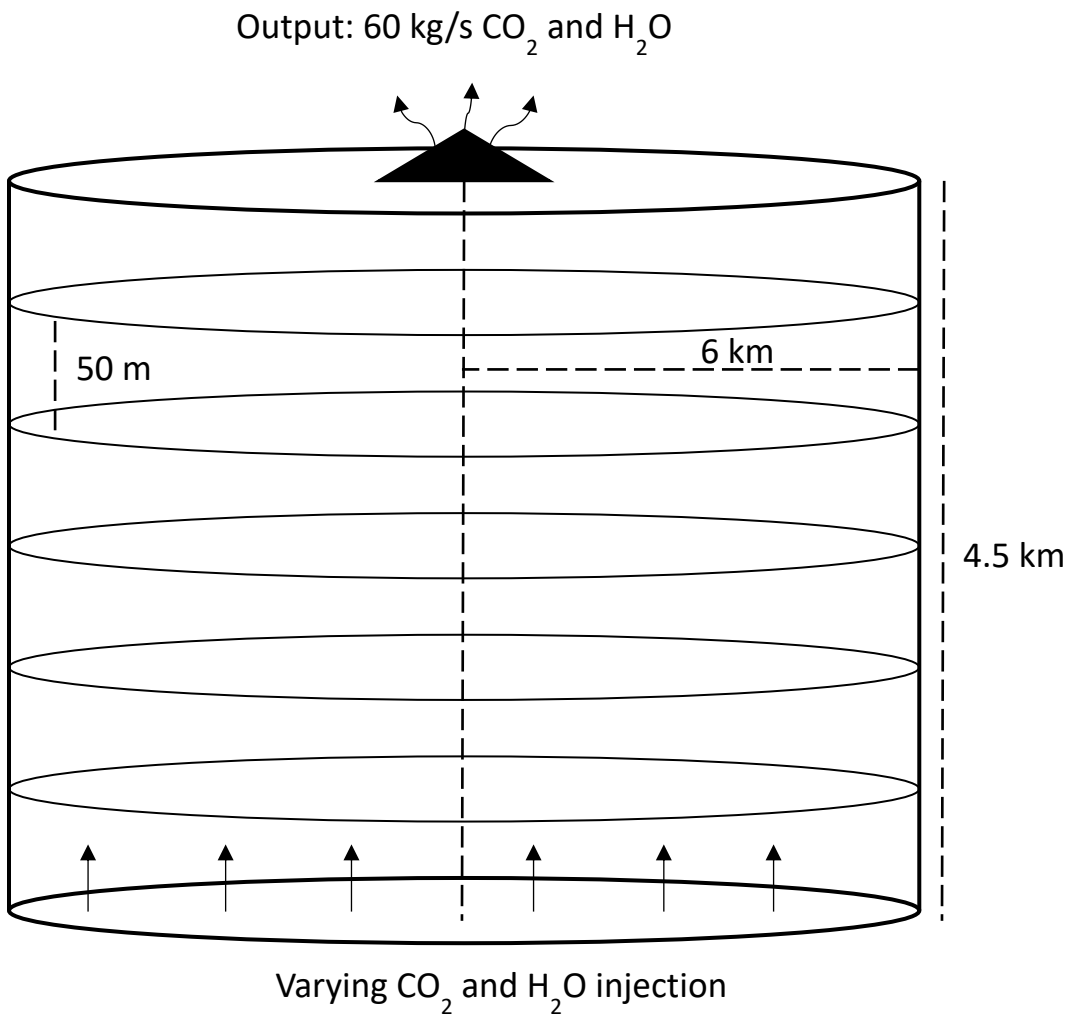

Figure 2.7: Diagram of the TOUGH3 model. The radius of the model was 6 km and the total height was 4.5 km split into ninety 50 m high sections. During the running of the model, the output from the system was kept at a constant 60 kg/s output of CO_2 and H_2O, while the CO_2 and H_2O input was varied for each model run.

After the initial conditions were set, the model was run to steady state with no injection. Steady state means that the simulation ran to the point where the parameters were no longer changing any appreciable amount, even for large time steps. This allowed the temperature and pressure to equilibrate across the entire model. Then the model was run numerous times while injecting varying amounts of CO_2 and H_2O, which corresponded to different H_2O/CO_2 molar ratios. Each model run had a set CO_2 and H_2O injection rate that remained constant for the entirety of the simulation. In total, four different scenarios were

simulated, each with a different H_2O/CO_2 molar ratio. The output file for each run gave information on the gaseous volume change, the PT conditions, and other phases and components present in the simulation.

2.2.4 Data collection and total CO_2 flux

The total CO_2 being emitted from Uturuncu was measured during a research expedition to the volcano in November, 2022. The soil accumulation chamber method was used to measure the CO_2 flux. This method measures the CO_2 accumulating in a chamber of known volume over a known time period in order to determine the flux of CO_2 (Chiodini et al., 1998). The EGM-5 portable CO_2 gas analyzer with attached soil respiration chamber from PP Systems was used for making individual flux measurements. If the CO_2 flux was high enough, the sensor would saturate before the instrument could determine the flux. When this happened, the CO_2 flux could still be calculated by recording the starting and ending CO_2 concentrations in the accumulation chamber over a chosen time period (1 minute). Equation 2.3 can be used to calculate the CO_2 flux, where α is the change in concentration of CO_2 in g/m^3 over the time. For cylindrical chambers, H_c is the height of the chamber (Chiodini et al., 1998).

Equation 2.3: $\phi_{soil\ CO2} = \alpha H_c$

A total of 698 flux measurements at three different locations on Uturuncu were made over a four-day period from Nov. 19th-22nd, 2022. Of these measurements, 160 were saturated and of the saturated measurements, the information required for determining the exact flux was collected for 29 of them. Each location had active fumaroles and heavily altered soil. A

previous CO_2 survey was conducted in 2018 that covered portions of the same locations (Fischer, unpublished). The 2022 CO_2 survey was used to update these numbers and provide a more comprehensive measurement of the total CO_2 being emitted from Uturuncu.

After collection of data in the field, the ArcGIS Geostatistical Wizard and the Gaussian Geostatistical Simulations (GGS) was used to interpolate between individual flux measurements and calculate a total flux for the entire field area. If the exact value of a saturated measurement was unknown, the median of the calculated saturated measurements was substituted in its place. Simple kriging was used to interpolate between data points and generate a map of these kriged values. This map was then used as input into the GGS in order to generate 10 simulation rasters and one mean statistical raster. The mean statistical raster was used to calculate the total CO_2 flux in tons/km^2/day for each site. These values were then converted to tons/day and added together in order to determine Uturuncu's total CO_2 flux. Further details about this method can be found in Rahilly and Fischer, 2021.

2.3 Results

2.3.1 Volume change

After constraining the LOS data to only the 40 km circle around Uturuncu and interpolating it, the volume change from 1992-2011 was 12.8×10^6 m^3/yr. This result accounts for both the radial and vertical deformation components. The same dataset but decomposed into its separate components resulted in a volume change of 14.5×10^6 m^3/yr based only on the vertical component of deformation. The total ΔV in m^3 was calculated by multiplying the ΔV by the years. Table 2.2 summarizes the volume change results for the 1992-2011 time period.

Table 2.2: Volume change results from 1992-2011.

ΔV (m^3/yr)	**Total ΔV (m^3)**	**Deformation component**
$12.8x10^6$	$2.47x10^8$	Vertical & radial
$14.5x10^6$	$2.85x10^8$	Vertical

Two ascending and two descending tracks that cover Uturuncu were available for the 2014-2017 time period. Figure 2.8 shows the vertical and radial deformation components for different combinations of the tracks. Additionally, by averaging the two ascending and then the two descending tracks, the average deformation components can be found (Figure 2.9). In order to compare the 1992-2011 time period to the 2014-2017 time period, the volume change for only the vertical component was determined for each track combination. The assumption was made that the ΔV from 2014-2017 is similar to the ΔV occurring today, so the total ΔV was calculated for 2014-2022. All of the volume change values are summarized in Table 2.3 and the average for the ascending and descending tracks was $1.3x10^6$ m^3/yr.

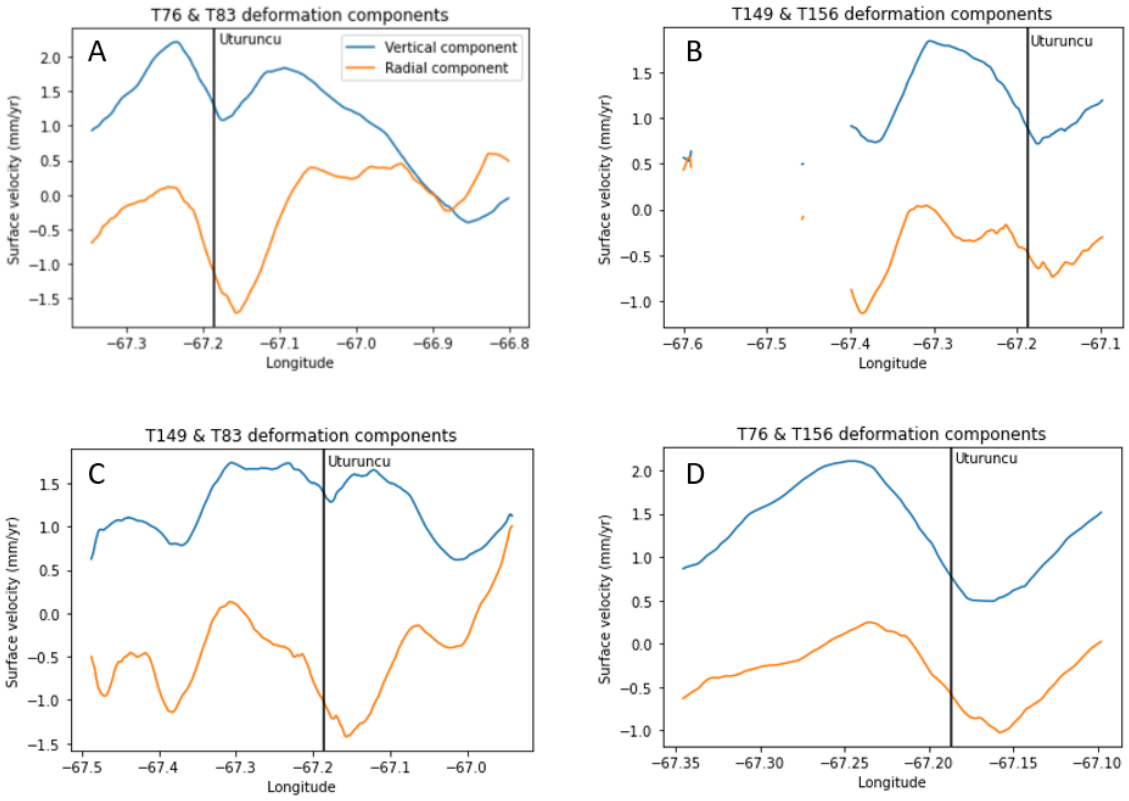

Figure 2.8: Vertical (blue) and radial (orange) deformation components for different combinations of ascending and descending tracks. Uturuncu's location is depicted with a vertical black line.

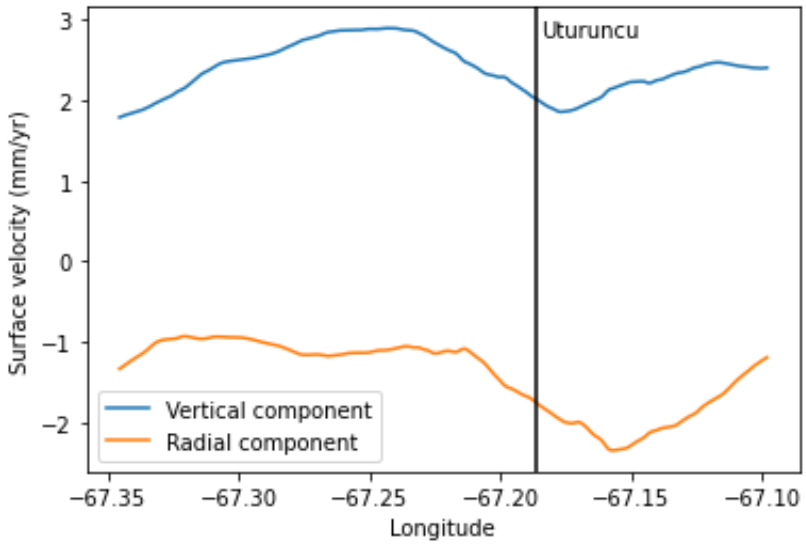

Figure 2.9: Average ascending and descending deformation components. Vertical is blue and radial is orange.

Table 2.3: Volume change results from 2014-2017.

ΔV (m^3/yr)	**Total ΔV (m^3)**	**Track**
$2.3x10^6$	$1.84x10^7$	T76 & T83
$1.2x10^6$	$9.6x10^6$	T149 & T156
$2.7x10^6$	$2.16x10^7$	T149 & T83
$7.7x10^5$	$6.16x10^6$	T76 & T156
$1.3x10^6$	$1.04x10^7$	Average of ascending and descending

2.3.2 VolatileCalc

For deep degassing from the APMB, the isobaric solubility curve for the rhyolite H_2O-CO_2 system was calculated with a pressure of 5000 bars and a temperature of 975 °C. An assumed H_2O wt% of 4.5 corresponds to ~2090 ppm CO_2 (Figure 2.10A). The open degassing path for a magma with a starting composition of 4.5 wt% H_2O and 2090 ppm CO_2 resulted in the molar ratios shown in Table 2.4, ranging from 0.42-8.5. The same process was repeated for shallow degassing from Uturuncu's most recent eruption (Figure 2.10B; Table 2.5) and the H_2O/CO_2 molar ratio ranged from 26.5-82.7.

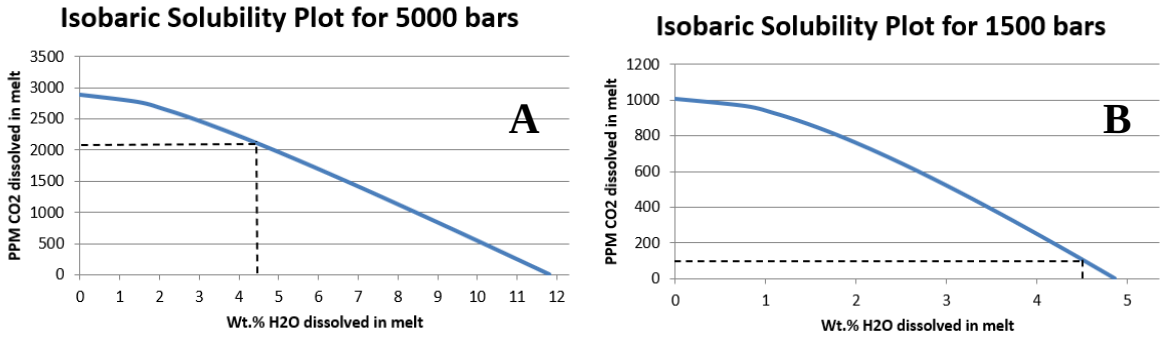

Figure 2.10: Isobaric solubility plots for deep degassing (A) and shallow degassing (B).

Table 2.4: Degassing for a deep magma with a starting composition of 4.5 wt% H_2O and 2090 ppm CO_2.

H_2Ov mol%	CO_2vmol%	H_2O/CO_2 (molar)
29.7	70.3	0.422833
30.6	69.4	0.441554
31.6	68.4	0.461798
32.6	67.4	0.483765
33.7	66.3	0.507698
34.8	65.2	0.53387
36.0	64.0	0.562616
37.3	62.7	0.594351
38.6	61.4	0.629592
40.1	59.9	0.668964
41.6	58.4	0.713259
43.3	56.7	0.763487
45.1	54.9	0.820968
47.0	53.0	0.887468
49.1	50.9	0.965356
51.4	48.6	1.057931
53.9	46.1	1.169913
56.7	43.3	1.308336
59.7	40.3	1.484069
63.2	36.8	1.71508
67.0	33.0	2.033083
71.4	28.6	2.499805
76.5	23.5	3.254376
82.4	17.6	4.688697
89.5	10.5	8.504741

Table 2.5: Degassing from a shallow magma.

H_2Ov mol%	CO_2vmol%	H_2O/CO_2 (molar)
96.4	3.6	26.49744
96.5	3.5	27.26161
96.6	3.4	28.08267
96.7	3.3	28.94378
96.8	3.2	29.85972

96.9	3.1	30.83544
97.0	3.0	31.87891
97.1	2.9	32.99551
97.2	2.8	34.1953
97.3	2.7	35.48583
97.4	2.6	36.87979
97.5	2.5	38.38819
97.6	2.4	40.02673
97.7	2.3	41.81349
97.8	2.2	43.7692
97.9	2.1	45.91784
98.0	2.0	48.29258
98.1	1.9	50.92807
98.2	1.8	53.87277
98.3	1.7	57.18186
98.4	1.6	60.92734
98.5	1.5	65.20629
98.6	1.4	70.13751
98.7	1.3	75.88254
98.8	1.2	82.66398

2.3.3 TOUGH3

Four different scenarios were run in TOUGH3 using the basic model setup described above and varying the H_2O/CO_2 molar ratio (Table 2.6). In the first scenario, only CO_2 was injected which represents very deep degassing. Scenario 2 has an H_2O/CO_2 molar ratio of 0.42, meaning that much more CO_2 is being injected than H_2O. This represents gas emissions from a younger, fresher magma that is still relatively undegassed. Scenario 3 has a H_2O/CO_2 molar ratio of 5 which is consistent with gases measured in Uturuncu fumaroles. Finally, scenario 4 has a H_2O/CO_2 molar ratio of 8.5 which represents an older magma that has already degassed most of its CO_2. For each scenario, multiple model runs were completed with gradually increasing amounts of CO_2 injection.

Table 2.6: Description of the four scenarios modeled in TOUGH3.

Scenario	H_2O/CO_2 molar	Description
1	Only CO_2	Very deep degassing
2	0.42	Degassing from a young, fresh magma that is still relatively undegassed
3	5	Actual conditions at Uturuncu, Bolivia
4	8.5	Degassing from an old magma that has already degassed most of its CO_2

In scenario 1, Figure 2.11A shows the maximum volume change for each model run when only CO_2 was being injected into the system. The amount of CO_2 injection was varied for each model run in order to determine how the ΔV changed. This figure shows that as CO_2 injection increases, the ΔV rapidly increases until approximately 2000 kg/s of CO_2 is being injected into the system. At this point, the ΔV curve flattens out and remains relatively constant no matter how much the CO_2 injection rate increases. This same pattern of rapid ΔV increase followed by a flattening out of the curve is repeated for the remaining 3 scenarios (Figure 2.11B, 2.11C, and 2.11D). However, the location of the inflection points as well as the slope of the curve changes for each scenario.

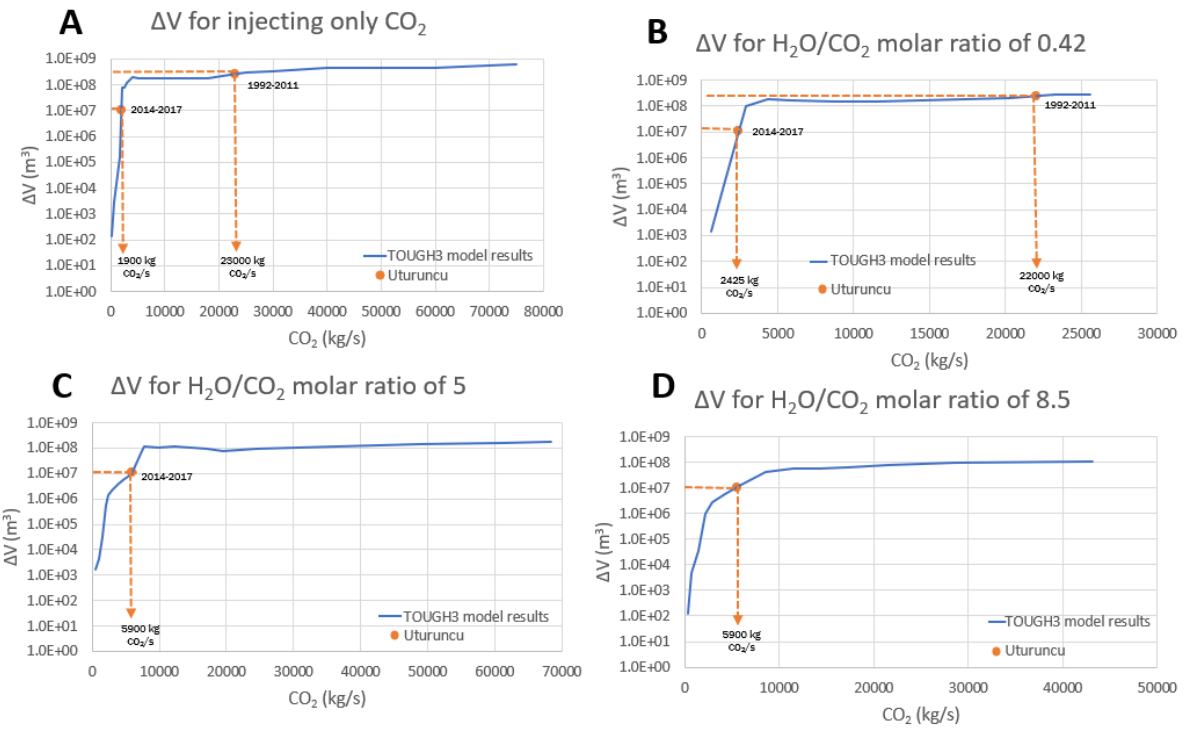

Figure 2.11: ΔV vs. the CO_2 injection for each scenario modeled in TOUGH3. The blue line represents the TOUGH3 model results and the orange dots represent the CO_2 injection required to produce the ΔV at Uturuncu. A-D represents scenarios 1-4.

Scenario 2 is similar to the first scenario because there is a rapid rise and then a sharp inflection point around 3000 kg CO_2/s where the curve flattens out (Figure 2.11B). However, scenarios 3 and 4 have a more gradual ΔV increase, which flattens out at approximately 7500 and 8500 kg CO_2/s respectively (Figure 2.11C and 2.11D). Overall, as the H_2O/CO_2 molar ratio increases, the slope of the graph before the inflection point decreases and the inflection point occurs at greater CO_2 injection rates.

These figures show the CO_2 injection rate required for producing a specific volume change in the Uturuncu hydrothermal system. The volume change required to cause the observed deformation has been calculated previously (Table 2.2 and Table 2.3). This information can be used to determine the required CO_2 injection rate into the hydrothermal system that will result in the volume change needed for producing the deformation observed at Uturuncu. From 1992-2011, Uturuncu was experiencing a higher uplift rate which required

a significantly larger volume change in order to accommodate the uplift. The ΔV from the TOUGH3 modeling only reached the larger volume change for scenarios 1 and 2. All four scenarios reached a ΔV for the lower uplift rates from 2014-2017. Tables 2.7-2.10 summarize the ΔV values for each scenario, whether the model reached steady state, and the total time the model ran. If the model did not reach steady state, it would run for 9999 time steps and then the simulation was halted. At this point, the time steps were only a fraction of an hour, so running the model would have been challenging and not have increased the final time by any appreciable amount.

Table 2.7: TOUGH3 model results when only CO_2 is injected into the hydrothermal system (scenario 1).

CO_2 (kg/s)	**ΔV (m^3)**	**Steady state?**	**Time (yrs)**
50	7.59	No	38.4
200	$2.56x10^2$	No	23.8
500	$5.19x10^3$	No	40.8
1600	$3.09x10^5$	No	41.1
2000	$1.55x10^8$	No	40.4
2500	$4.28x10^5$	No	29.2
3000	$2.25x10^8$	No	27.2
4000	$1.84x10^8$	No	26.5
5000	$1.79x10^8$	No	22.7
7500	$1.68x10^8$	No	18.4
9000	$1.91x10^8$	No	15.4
12000	$1.68x10^8$	No	11.3
18000	$2.05x10^8$	No	5.8
22000	$2.75x10^8$	No	5.8
25000	$3.33x10^8$	No	4.7
30000	$3.53\ x10^8$	No	5.7

40000	$5.05x10^8$	No	4.9
50000	$3.68x10^8$	No	8.8
60000	$5.49x10^8$	No	3.7
75000	$6.19x10^8$	No	9

Table 2.8: TOUGH3 model results for scenario 2 (H_2O/CO_2 molar ratio is 0.42).

H_2O (kg/s)	**CO_2 (kg/s)**	**ΔV (m^3)**	**Steady state?**	**Time (yrs)**
50	290.7483748	$6.72x10^2$	No	32.9
100	581.4967496	$2.27x10^3$	No	40.3
250	1453.741874	$1.70x10^5$	Yes	43904
500	2907.483748	$1.90x10^8$	No	28.3
750	4361.225622	$1.75x10^8$	No	20.7
1000	5814.967496	$1.52x10^8$	No	20.7
1500	8722.451245	$1.44x10^8$	No	15.3
2000	11629.93499	$1.55x10^8$	No	11.5
2500	14537.41874	$1.72x10^8$	No	7.9
3500	20352.38624	$2.55x10^8$	No	5.3
4000	23259.86999	$2.80x10^8$	No	4.7
4400	25585.85698	$3.03x10^8$	No	4.1

Table 2.9: TOUGH3 model results for scenario 3 (H_2O/CO_2 molar ratio is 5).

H_2O (kg/s)	**CO_2 (kg/s)**	**ΔV (m^3)**	**Steady state?**	**Time (yrs)**
100	48.84573	0	No	23.6
500	244.2286	$4.07x10^2$	No	25.2
1000	488.4573	$2.87x10^3$	No	35
2000	976.9145	$5.37x10^3$	No	37
3000	1465.372	$5.60x10^4$	No	39.3
4000	1953.829	$1.01x10^6$	Yes	20942
5000	2442.286	$1.68x10^6$	Yes	26290

6000	2930.744	$2.52x10^6$	Yes	5831
7000	3419.201	$3.53x10^6$	Yes	39357
8000	3907.658	$4.72x10^6$	Yes	29148
10000	4884.573	$7.61x10^6$	Yes	41204
12000	5861.487	$1.12x10^7$	Yes	20540
15000	7326.859	$1.34x10^8$	No	14.3
16000	7815.316	$8.94x10^7$	No	15.3
20000	9769.145	$1.25x10^8$	No	12
25000	12211.43	$1.11x10^8$	No	10.4
35000	17096	$7.35x10^7$	Yes	60965
40000	19538.29	$8.48x10^7$	Yes	76828
50000	24422.86	$1.04x10^8$	Yes	136514
75000	36634.3	$1.36x10^8$	Yes	176986
100000	48845.73	$1.59x10^8$	Yes	152376
125000	61057.16	$1.75Ex10^8$	Yes	140960
140000	68384.02	$1.83x10^8$	Yes	410996

Table 2.10: TOUGH3 model results for scenario 4 (H_2O/CO_2 molar ratio is 8.5).

H_2O (kg/s)	**CO_2 (kg/s)**	**ΔV (m^3)**	**Steady state?**	**Time (yrs)**
50	14.36639029	0	No	91.3
500	143.6639029	1.46	No	16.5
1000	287.3278057	$2.35x10^2$	No	19.4
2500	718.3195143	$9.31x10^3$	No	28.8
5000	1436.639029	$6.31x10^4$	No	34.2
7500	2154.958543	$1.92x10^6$	Yes	22878
10000	2873.278057	$3.62x10^6$	Yes	26388
15000	4309.917086	$8.55x10^6$	Yes	31064
20000	5746.556114	$1.53x10^7$	Yes	31681
30000	8619.834171	$7.12x10^7$	No	13.1

40000	11493.11223	$4.89x10^7$	Yes	92726
50000	14366.39029	$6.29x10^7$	Yes	6823
60000	17239.66834	$7.41x10^7$	Yes	125566
75000	21549.58543	$8.68x10^7$	Yes	76991
100000	28732.78057	$1.02x10^7$	Yes	59180
150000	43099.17086	$1.18x10^7$	Yes	121920

2.3.4 Total CO_2 flux

Figure 2.12 shows the CO_2 flux data points in $g/m^2/day$ for each of the three sites surveyed during the November, 2022 expedition. Interpolation was performed for the data points at each site and the resulting maps were used as inputs to the GGS tool in ArcGIS (Figure 2.13). Site 1 had a total CO_2 flux of 45.74 tons/day or 798.9 $tons/km^2/day$ when using the total area of the site. Site 2 had a total flux of 29.05 tons/day or 1282.9 $tons/km^2/day$ and Site 3 had a total flux of 88.3 tons/day or 765.8 $tons/km^2/day$. For the three areas that were measured, the cumulative CO_2 flux is 163.09 tons/day.

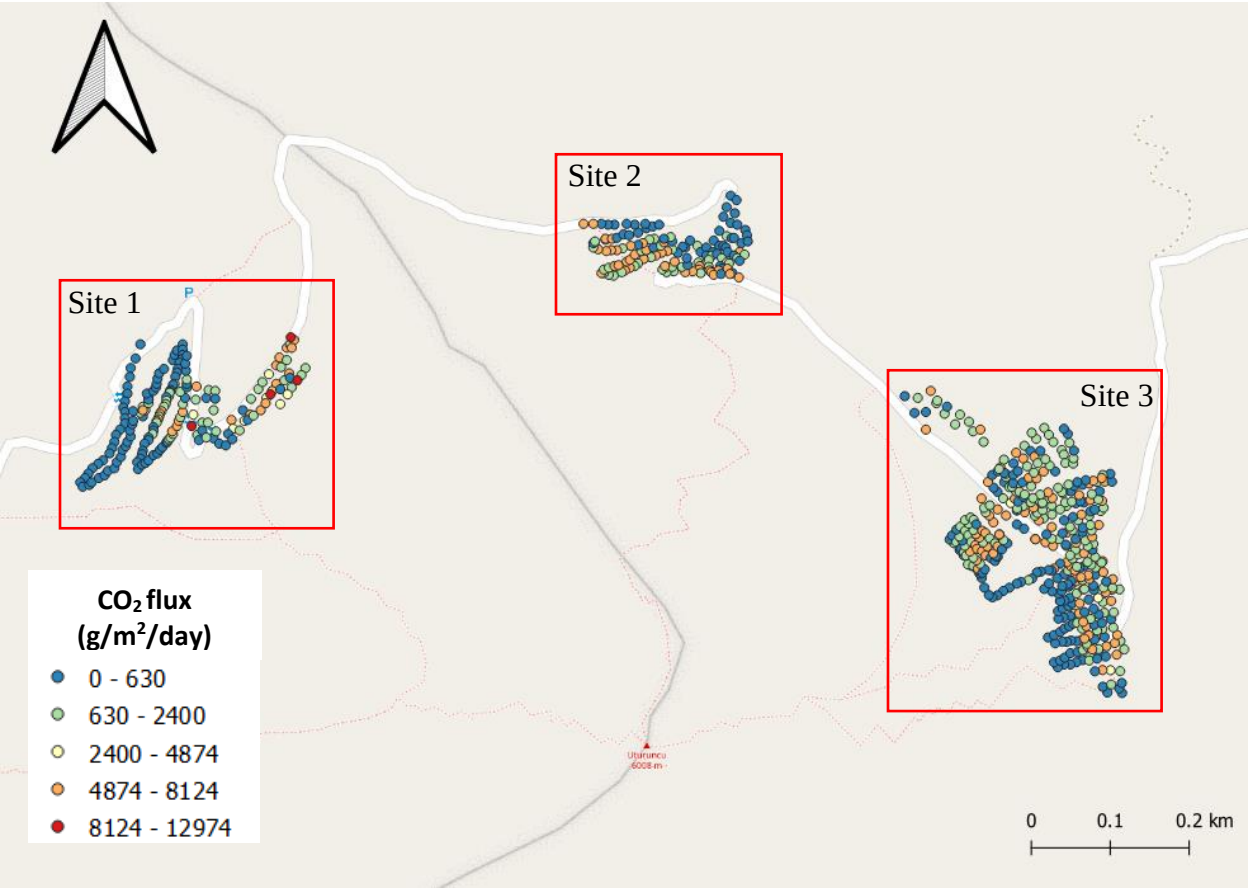

Figure 2.12: CO_2 flux measurements for the three sites surveyed during the November, 2022 expedition.

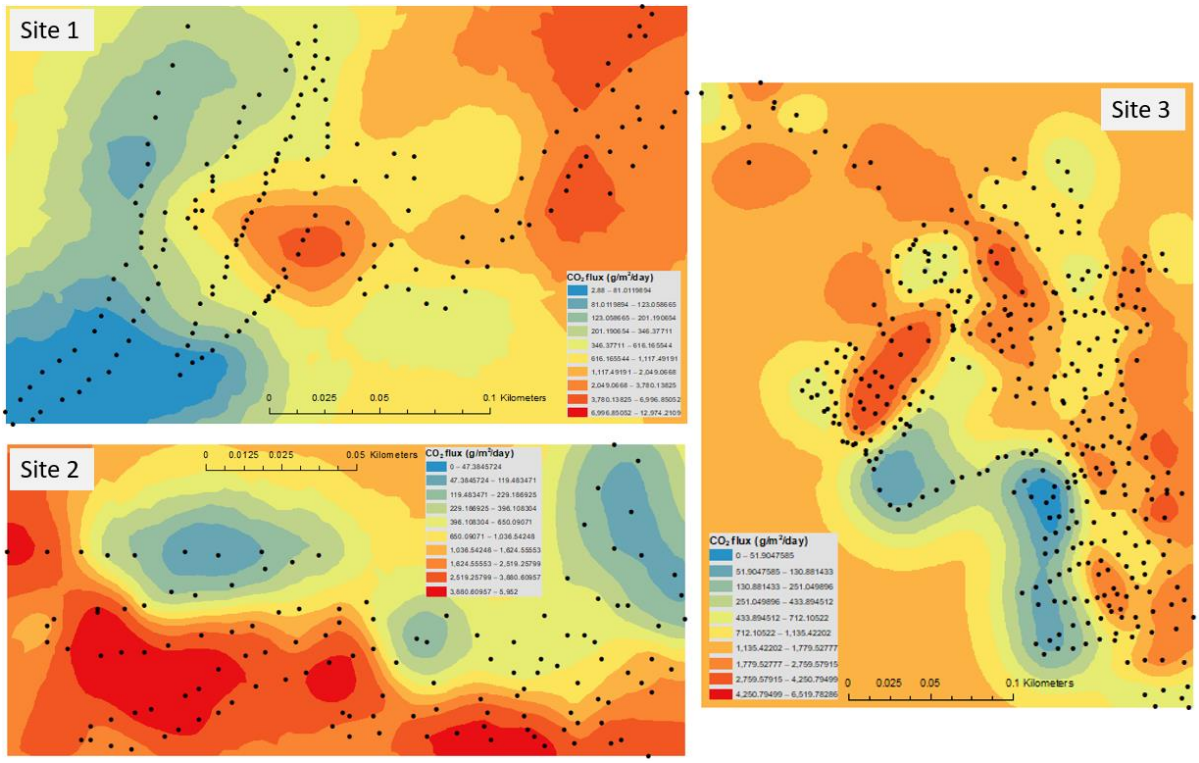

Figure 2.13: Kriged CO_2 flux data for sites 1-3. The measurement points are displayed as black dots at each site

2.4 Discussion

2.4.1 Volume change

Calculating the volume change based on InSAR data only calculates the volume change at the surface. The primary assumption behind these calculations is that the volume change at the surface is the same as the volume change at the depth of the hydrothermal system. Factors such as rock compressibility and increasing pressure are considered negligible in this scenario.

InSAR is advantageous because it can record data during both the day and night and can see through cloud cover (Ding et al., 2008). However, the accuracy of the data can also be impacted by atmospheric noise and vegetation effects (Ding et al., 2008; Westerhoff and Steyn-Ross, 2020). These gaps in the data from Uturuncu can be seen in Figure 2.6 and Figure 2.8. Very little vegetation can be found on and around Uturuncu due to the high elevation. Because of this, it is likely that gaps in the data are caused by atmospheric noise and not by vegetation effects.

The results of these calculations show that there is an order of magnitude decrease in the volume change between the 1992-2011 data and the 2014-2017 data. This makes sense because as the uplift rate decreases, the volume change would also be expected to decrease. For the 1992-2011 data, the volume change calculated based only on the vertical deformation component is slightly higher than the combined vertical and radial component volume change. The combined volume calculation takes into account the outwards movement in addition to the upwards movement, so the overall volume change is lower than if only the

upwards movement is considered. The data for 2014-2017 varies between $6.16x10^6$ and $2.16x10^7$ m^3 with an average value of $1.04x10^7$ m^3.

2.4.2 TOUGH3

The results from the Tough3 modeling provide an estimate of the amount of CO_2 injection required to produce varying volume changes and these numbers are summarized in Tables 2.11-2.14.

Table 2.11: The CO_2 injection required to cause the ΔV at Uturuncu in scenario 1.

ΔV from InSAR data (m^3)	**CO_2 injection (kg/s)**	**Years**
$2.47x10^8$	23000	1992-2011
$2.85x10^8$	25000	1992-2011
$6.16x10^6$	1800	2014-2017
$9.60x10^6$	1900	2014-2017
$1.04x10^7$	1900	2014-2017
$1.84x10^7$	1925	2014-2017
$2.16x10^7$	1975	2014-2017

Table 2.12: The CO_2 injection required to cause the ΔV at Uturuncu in scenario 2.

ΔV from InSAR data (m^3)	**CO_2 injection (kg/s)**	**Years**
$2.47x10^8$	22000	1992-2011
$2.85x10^8$	25000	1992-2011
$6.16x10^6$	2300	2014-2017
$9.60x10^6$	2400	2014-2017
$1.04x10^7$	2425	2014-2017
$1.84x10^7$	2500	2014-2017
$2.16x10^7$	2525	2014-2017

Table 2.13: The CO_2 injection required to cause the ΔV at Uturuncu in scenario 3.

ΔV from InSAR data (m^3)	**CO_2 injection (kg/s)**	**Years**
$2.47x10^8$	None	1992-2011
$2.85x10^8$	None	1992-2011
$6.16x10^6$	5000	2014-2017
$9.60x10^6$	5600	2014-2017
$1.04x10^7$	5900	2014-2017
$1.84x10^7$	6300	2014-2017
$2.16x10^7$	6400	2014-2017

Table 2.14: The CO_2 injection required to cause the ΔV at Uturuncu in scenario 4.

ΔV from InSAR data (m^3)	**CO_2 injection (kg/s)**	**Years**
$2.47x10^8$	None	1992-2011
$2.85x10^8$	None	1992-2011
$6.16x10^6$	4500	2014-2017
$9.60x10^6$	5400	2014-2017
$1.04x10^7$	5600	2014-2017
$1.84x10^7$	6900	2014-2017
$2.16x10^7$	7300	2014-2017

For scenario 1 (Table 2.11), when only CO_2 is being injected into the system, the CO_2 injection rate required to match the ΔV from InSAR data remains just below 2000 kg/s for the 2014-2017 time period. This number increases to 23000+ kg/s for the 1992-2011 time period. There are similar results for scenario 2 (Table 2.12), with between 2300 and 2525 kg/s of CO_2 being injected from 2014-2017 and 22000+ kg/s from 1992-2011. However, the CO_2 injection rate for 2014-2017 increases to 5000-6400 kg/s for scenario 3 (Table 2.13) and 4500-7300 kg/s for scenario 4 (Table 2.14). At the same time, there is no longer a CO_2

injection rate from 1992-2011 that could match the volume change calculated based on the InSAR data for either scenario.

Overall, for each scenario, there is some amount of CO_2 that can be injected in order to produce the uplift observed from 2014-2017. Significantly more CO_2 needs to be injected to produce the 1992-2011 volume change and based on the model results, this can only occur in Scenarios 1 and 2 (Table 2.11 and 2.12). In Scenarios 3 and 4, the curve flattens out before reaching the necessary volume changes. For scenarios 2-4, water is also being injected into the system in addition to CO_2. The water injection rates are included in Tables 2.8-2.10. These water amounts are included in the volume change, but only CO_2 injection rates are discussed in detail for this project.

To put these CO_2 injection numbers into context, they can be compared to the amount of CO_2 degassing from active volcanos around the world (Figure 2.14). Etna is emitting approximately 3000 kt/yr of CO_2 or ~100 kg CO_2/s (Fischer et al., 2019). According to the data collected during the 2022 expedition, Uturuncu is emitting between 12.3 and 20.6 kg CO_2/s. Comparing these numbers to Figure 2.14, Uturuncu would plot at a similar location to San Cristobal. This number accounts for the diffuse degassing from Uturuncu's summit, while many of the volcanos on this chart either do not exhibit diffuse degassing or it has not been measured. For scenario 3, from 2014-2017, 5900 kg CO_2/s were injected to produce the average volume change of 1.04×10^7 m^3. This means that based on Etna's yearly CO_2 degassing rate of 100 kg/s, the Uturuncu system would need to be injecting 59 Etna's worth of CO_2 in order to match the volume change from the InSAR data. However, there is no amount of injected CO_2 that would result in the volume change from 1992-2011. If only CO_2,

and no H_2O, was being injected into the system (scenario 1) from 1992-2011, then at least 230 Etna's worth of CO_2 would need to be injected. This is a significant amount of CO_2, but the APMB has a volume of ~500,000 km^3, and could produce a large amount of CO_2 (Pritchard et al., 2018).

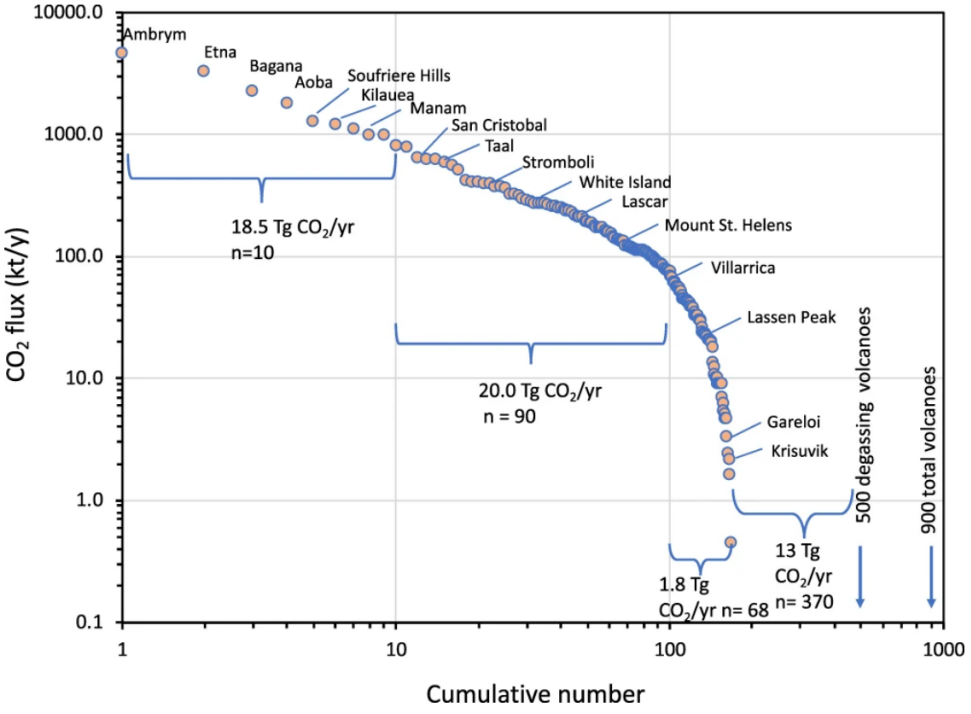

Figure 2.14: CO_2 flux for volcanos around the world (Fischer et al., 2019).

An estimate of the APMB CO_2 content can be made by knowing its volume and the CO_2 wt%, which is assumed to be 0.15 wt% CO_2. The APMB has a radius of 100 km and a height of 10-20 km, which results in a volume range of $3.14x10^5$-$6.28x10^5$ km^3 (Pritchard et al., 2018). Based on this, the total mass of CO_2 in the APMB is $1.24x10^{15}$-$2.48x10^{15}$ kg. Injecting 6400 kg CO_2/s from 2014 to the current year is a total of $1.62x10^{12}$ kg of CO_2 injected into Uturuncu's hydrothermal system. Injecting 25,000 kg CO_2/s over the 19-year period from 1992-2011 results in a total of $1.50x10^{13}$ kg of CO_2 injected. So, the APMB

theoretically contains enough CO_2 to cover what needs to be injected to produce both the low uplift rates observed from 2014-2017 and the higher uplift rates observed from 1992-2011.

However, it is unlikely that the entirety of the APMB supplies volatiles to the hydrothermal system beneath Uturuncu. The volume of the APMB located directly beneath the model is only a small portion of the total volume, ranging from 1131-2262 km^3. In this case, the mass of CO_2 in this portion of the APMB is $8.92x10^{12}$ kg. This is enough CO_2 to produce the uplift from 2014-2017, but it does not cover the $1.50x10^{13}$ kg of CO_2 required for the uplift from 1992-2011. While there is potentially enough CO_2 present in the APMB to supply the hydrothermal system from 2014 to present day, it would require the unlikely scenario of nearly all the CO_2 degassing over an 8-year period. Because of this, the cause of Uturuncu's deformation may be a combination of volatile movement in the hydrothermal system and magma movement.

Each scenario modeled in TOUGH3 accounts for magmas degassing from different depths and for differing periods of time. Scenario 1 and 2 both represent deep degassing where significantly more CO_2 is being degassed than H_2O. In both cases, there is a certain point where the volume change reaches a value that matches the high uplift rate from 1992-2011. However, as the H_2O/CO_2 molar ratio increases to 5 and 8.5 (scenarios 3 and 4), the volume change curve never reaches the values required for the high uplift rate. This is based only on the CO_2 injected into the system, and does not consider the H_2O. In order for the uplift from 1992-2011 to be caused purely by CO_2 injection, there would need to be degassing from a very deep source that is emitting far more CO_2 than H_2O. Gas

measurements at Uturuncu fumaroles indicate an H_2O/CO_2 ratio of 5 which is not consistent with the requirements.

In Figure 2.11, the ΔV_{max} curve flattens out and reaches a relatively constant rate for each scenario. This means that after a certain point, no matter how much CO_2 is injected into the system, the volume of the system remains unchanged. Something must be happening to account for all of the injected CO_2 if it is not changing the volume of the hydrothermal system. One possible explanation for this is carbon mineralization. This occurs when CO_2 reacts with rocks rich in calcium or magnesium to form solid carbonate minerals, such as calcite, dolomite, or magnesite (Kelemen et al., 2019; Neeraj and Yadav, 2020; Snaebjörnsdóttir et al., 2020). The reaction would trap the CO_2 and prevent it from further increasing the volume of the hydrothermal system. TOUGH3 does not provide information about other possible minerals forming in the injection system, so while carbon mineralization may be occurring in the system, it cannot be proven based on the information provided by TOUGH3.

Another important factor to consider is the depth and size of the deformation source and how that impacts the surface expression of the deformation. Source geometries influence the extent and shape of deformation at the surface (Yang et al., 1988; Fialko et al., 2001; Pritchard and Simons, 2004; Barone et al., 2019). Generally, a large and wide surface deformation could be caused either by a deep, smaller source or a shallow, larger source. The modeling during this research focuses on a small deformation source (Uturuncu's hydrothermal system) and attempts to use volatile movement into this system to explain the widespread deformation around Uturuncu's summit. Such a small, shallow deformation

source likely could not cause such a large uplift, but it may contribute to the uplift around the central region where Uturunu's summit is located.

2.4.3 Total CO_2 flux

Of the three sites surveyed during the 2022 expedition, Site 2 was emitting the most CO_2, at 1282.9 tons/km^2/day. The other two sites were emitting similar amounts of CO_2 to each other and about 400 tons/km^2/day less than the amount produced at Site 2. Large portions of the volcano are visibly emitting gas or have heavily altered rock and soil and only a comparatively small portion of these areas were able to be measured during the expedition. However, these measurements can be used to estimate the total CO_2 from the volcano.

The approximate total area of altered soil and rock is 1.53 km^2, estimated from Google Earth images of Uturuncu. Using this area, the total CO_2 flux from Uturuncu is 1172-1963 tons/day or 12.3-20.6 kg CO_2/s. The same measurements completed in 2018, but with fewer data points, resulted in a CO_2 flux of 16.1-20.6 kg/s. These measurements are very similar and in the context of the Tough3 model, adjusting the CO_2 output based on the new data will result in miniscule changes because the input to the system greatly outweighs the output. The new data from 2022 provides more detailed knowledge of the volcano and these updated numbers will be used in future models and projects.

These are significant CO_2 emission values for a volcano that has not erupted in 250,000 years. As a comparison, Yellowstone is emitting 24 ± 12 kt/day of CO_2 from altered soil around the National Park (Rahilly and Fischer, 2021). Yellowstone last erupted ~70,000 years ago but the hydrothermal system is still highly active (Christiansen et al., 2007).

Uturuncu has not erupted in almost quadruple that amount of time, but also appears to have an active hydrothermal system that is degassing nearly 2 kt CO_2/day.

2.5 Conclusions

For decades, Uturuncu has been experiencing deformation at varying rates. Before 2011, an area with a radius of 40 km was uplifting at ~ 1 cm/yr, but this dropped to 2-3 mm/yr since then. Deformation at volcanos is typically thought to be caused by magma movement but volatiles moving into and getting trapped in Uturuncu's hydrothermal system could be another explanation. TOUGH3 was used to model this volatile movement in order to determine the feasibility of this hypothesis. It was found that a significant amount of CO_2 would need to be injected into the hydrothermal system to cause the observed uplift.

The 2-3 mm/yr of uplift in recent years would require injecting 5900 kg CO_2/s which equates to the yearly CO_2 output from 59 Etna's. This is a significant amount of CO_2, but the APMB is one of the largest magma bodies on Earth and the portion beneath Uturuncu's hydrothermal system contains sufficient CO_2 to supply that amount of input to the system. However, the higher deformation before 2011 would require closer to 230 Etna's worth of CO_2 being injected. The CO_2 in the portion of the APMB beneath the hydrothermal system would not be enough to support that large of an input to the system. Movement of volatiles and gases getting trapped in Uturuncu's hydrothermal system could be the sole reason for the current deformation observed at the volcano. However, based on the modeling in TOUGH3, before 2011 volatiles by themselves would not be able to create a large enough volume change in the hydrothermal system. Therefore, some other factor (e.g. magma movement)

would have been required to produce the observed uplift. The most plausible cause behind the deformation is likely a combination of the two end member scenarios. Likely both magma movement and volatile movement in Uturuncu's hydrothermal system contribute to the observed deformation. Uturuncu has not erupted in 250,000 years, but it continues to deform around the summit and release almost 2000 tons/day of CO_2, indicating that this volcano is not dead and remains important to study.

Acknowledgements

This work was supported by NSF award #1757415 from the NSFGEO-NERC program. Special thanks to Eric Lindsey at the University of New Mexico for helping with calculating the volume change using InSAR data. Additional thanks to Christine Doughty and Yingqi Zhang at Lawrence Berkley National Laboratory for assistance with the TOUGH3 modeling.

References

Allmendinger, R.W., Jordan, T.E., Kay, S.M., and Isacks, B.L., 1997, THE EVOLUTION OF THE ALTIPLANO-PUNA PLATEAU OF THE CENTRAL ANDES: Annual Review of Earth and Planetary Sciences, v. 25, p. 139–174, doi:10.1146/annurev.earth.25.1.139.

Barone, A., Fedi, M., Tizzani, P., and Castaldo, R., 2019, Multiscale Analysis of DInSAR Measurements for Multi-Source Investigation at Uturuncu Volcano (Bolivia): Remote Sensing, v. 11, p. 703, doi:10.3390/rs11060703.

Brenguier, F., Shapiro, N.M., Campillo, M., Ferrazzini, V., Duputel, Z., Coutant, O., and Nercessian, A., 2008, Towards forecasting volcanic eruptions using seismic noise: Nature Geoscience, v. 1, p. 126–130, doi:10.1038/ngeo104.

Capitanio, F.A., Faccenna, C., Zlotnik, S., and Stegman, D.R., 2011, Subduction dynamics and the origin of Andean orogeny and the Bolivian orocline: Nature, v. 480, p. 83–86, doi:10.1038/nature10596.

Cashman, K.V., and Hoblitt, R.P., 2004, Magmatic precursors to the 18 May 1980 eruption of Mount St. Helens, USA: Geology, v. 32, p. 141–144, doi:10.1130/G20078.1.

Chiodini, G., Cioni, R., Guidi, M., Raco, B., and Marini, L., 1998, Soil CO2 flux measurements in volcanic and geothermal areas: Applied Geochemistry, v. 13, p. 543–552, doi:10.1016/S0883-2927(97)00076-0.

Chmielowski, J., Zandt, G., and Haberland, C., 1999, The Central Andean Altiplano-Puna magma body: Geophysical Research Letters, v. 26, p. 783–786, doi:10.1029/1999GL900078.

Christiansen, R., Lowenstern, J., Smith, R., Heasler, H., Morgan, L., Nathanson, M., Mastin, L., Muffler, P., and Robinson, 2007, Preliminary assessment of volcanic and hydrothermal hazards in Yellowstone National Park and vicinity: Open-File Report Open-File Report.

Comeau, M.J., Unsworth, M.J., and Cordell, D., 2016, New constraints on the magma distribution and composition beneath Volcán Uturuncu and the southern Bolivian Altiplano from magnetotelluric data: Geosphere, v. 12, p. 1391–1421, doi:10.1130/GES01277.1.

Ding, X., Li, Z., Zhu, J., Feng, G., and Long, J., 2008, Atmospheric Effects on InSAR Measurements and Their Mitigation: Sensors (Basel, Switzerland), v. 8, p. 5426–5448, doi:10.3390/s8095426.

Edmonds, M., and Wallace, P.J., 2017, Volatiles and Exsolved Vapor in Volcanic Systems: Elements, v. 13, p. 29–34, doi:10.2113/gselements.13.1.29.

Fialko, Y., Khazan, Y., and Simons, M., 2001, Deformation due to a pressurized horizontal circular crack in an elastic half-space, with applications to volcano geodesy: Geophysical Journal International, v. 146, p. 181–190, doi:10.1046/j.1365-246X.2001.00452.x.

Fialko, Y., and Pearse, J., 2012, Sombrero Uplift Above the Altiplano-Puna Magma Body: Evidence of a Ballooning Mid-Crustal Diapir: Science, v. 338, p. 250–252, doi:10.1126/science.1226358.

Fischer, T.P. et al., 2019, The emissions of CO2 and other volatiles from the world's subaerial volcanoes: Scientific Reports, v. 9, p. 18716, doi:10.1038/s41598-019-54682-1.

Fischer, T.P., and Chiodini, G., 2015, Chapter 45 - Volcanic, Magmatic and Hydrothermal Gases, *in* Sigurdsson, H. ed., The Encyclopedia of Volcanoes (Second Edition), Amsterdam, Academic Press, p. 779–797, doi:10.1016/B978-0-12-385938-9.00045-6.

Gottsmann, J., Blundy, J., Henderson, S., Pritchard, M.E., and Sparks, R.S.J., 2017, Thermomechanical modeling of the Altiplano-Puna deformation anomaly: Multiparameter insights into magma mush reorganization: Geosphere, v. 13, p. 1042–1065, doi:10.1130/GES01420.1.

Henderson, S.T., and Pritchard, M.E., 2013, Decadal volcanic deformation in the Central Andes Volcanic Zone revealed by InSAR time series: Geochemistry, Geophysics, Geosystems, v. 14, p. 1358–1374, doi:https://doi.org/10.1002/ggge.20074.

Henderson, S.T., and Pritchard, M.E., 2017, Time-dependent deformation of Uturuncu volcano, Bolivia, constrained by GPS and InSAR measurements and implications for source models: Geosphere, v. 13, p. 1834–1854, doi:10.1130/GES01203.1.

Jung, Y., Pau, G.S.H., Finsterle, S., and Doughty, C., 2018, TOUGH3 User's Guide:

Kelemen, P., Benson, S.M., Pilorgé, H., Psarras, P., and Wilcox, J., 2019, An Overview of the Status and Challenges of CO2 Storage in Minerals and Geological Formations: Frontiers in Climate, v. 1, https://www.frontiersin.org/articles/10.3389/fclim.2019.00009 (accessed December 2022).

Kukarina, E., West, M., Keyson, L.H., Koulakov, I., Tsibizov, L., and Smirnov, S., 2017, Focused magmatism beneath Uturuncu volcano, Bolivia: Insights from seismic tomography and deformation modeling: Geosphere, v. 13, p. 1855–1866, doi:10.1130/GES01403.1.

Lau, N., Tymofyeyeva, E., and Fialko, Y., 2018a, Variations in the long-term uplift rate due to the Altiplano–Puna magma body observed with Sentinel-1 interferometry: Earth and Planetary Science Letters, v. 491, p. 43–47, doi:10.1016/j.epsl.2018.03.026.

Lau, N., Tymofyeyeva, E., and Fialko, Y., 2018b, Variations in the long-term uplift rate due to the Altiplano–Puna magma body observed with Sentinel-1 interferometry: Earth and Planetary Science Letters, v. 491, p. 43–47, doi:10.1016/j.epsl.2018.03.026.

MacQueen, P., Gottsmann, J., Pritchard, M.E., Young, N., Ticona J, F., Ticona, E. (Tico), and Tintaya, R., 2021, Dissecting a Zombie: Joint Analysis of Density and Resistivity Models Reveals Shallow Structure and Possible Sulfide Deposition at Uturuncu Volcano, Bolivia: Frontiers in Earth Science, v. 9, p. 755, doi:10.3389/feart.2021.725917.

Neeraj, and Yadav, S., 2020, Carbon storage by mineral carbonation and industrial applications of CO2: Materials Science for Energy Technologies, v. 3, p. 494–500, doi:10.1016/j.mset.2020.03.005.

Newman, S., and Lowenstern, J.B., 2002, VolatileCalc: a silicate melt–H2O–CO2 solution model written in Visual Basic for excel: Computers & Geosciences, v. 28, p. 597–604, doi:10.1016/S0098-3004(01)00081-4.

Pan, L., Spycher, N., Doughty, C., and Pruess, K., 2015, ECO2N V2.0: A TOUGH2 Fluid Property Module for Mixtures of Water, NaCl, and CO2:

Prezzi, C.B., Götze, H.-J., and Schmidt, S., 2009, 3D density model of the Central Andes: Physics of the Earth and Planetary Interiors, v. 177, p. 217–234, doi:10.1016/j.pepi.2009.09.004.

Pritchard, M.E. et al., 2018, Synthesis: PLUTONS: Investigating the relationship between pluton growth and volcanism in the Central Andes: Geosphere, v. 14, p. 954–982, doi:10.1130/GES01578.1.

Pritchard, M.E., and Simons, M., 2004, An InSAR-based survey of volcanic deformation in the central Andes: Geochemistry, Geophysics, Geosystems, v. 5, doi:10.1029/2003GC000610.

Rahilly, K.E., and Fischer, T.P., 2021, Total diffuse CO2 flux from Yellowstone caldera incorporating high CO2 emissions from cold degassing sites: Journal of Volcanology and Geothermal Research, p. 107383, doi:10.1016/j.jvolgeores.2021.107383.

Rouwet, D., Sandri, L., Marzocchi, W., Gottsmann, J., Selva, J., Tonini, R., and Papale, P., 2014, Recognizing and tracking volcanic hazards related to non-magmatic unrest: a review: Journal of Applied Volcanology, v. 3, p. 17, doi:10.1186/s13617-014-0017-3.

Silva, S.L. de, 1989, Altiplano-Puna volcanic complex of the central Andes: Geology, v. 17, p. 1102–1106, doi:10.1130/0091-7613(1989)017<1102:APVCOT>2.3.CO;2.

Snaebjörnsdóttir, S.Ó., Sigfússon, B., Marieni, C., Goldberg, D., Gíslason, S.R., Oelkers, E.H., and Snæbjörnsdóttir, S.Ó., 2020, Carbon dioxide storage through mineral carbonation: Nature Reviews Earth & Environment, v. 1, p. 90–102, doi:10.1038/s43017-019-0011-8.

Sparks, R.S.J., 2003, Forecasting volcanic eruptions: Earth and Planetary Science Letters, v. 210, p. 1–15, doi:10.1016/S0012-821X(03)00124-9.

Sparks, R.S.J., Folkes, C.B., Humphreys, M.C.S., Barfod, D.N., Clavero, J., Sunagua, M.C., McNutt, S.R., and Pritchard, M.E., 2008, Uturuncu volcano, Bolivia: Volcanic unrest due to mid-crustal magma intrusion: American Journal of Science, v. 308, p. 727–769, doi:10.2475/06.2008.01.

Vivo, B.D., Lima, A., and Webster, J.D., 2005, Volatiles in Magmatic-Volcanic Systems: Elements, v. 1, p. 19–24, doi:10.2113/gselements.1.1.19.

Westerhoff, R., and Steyn-Ross, M., 2020, Explanation of InSAR Phase Disturbances by Seasonal Characteristics of Soil and Vegetation: Remote Sensing, v. 12, p. 3029, doi:10.3390/rs12183029.

Yang, X.-M., Davis, P.M., and Dieterich, J.H., 1988, Deformation from inflation of a dipping finite prolate spheroid in an elastic half-space as a model for volcanic stressing: Journal of Geophysical Research: Solid Earth, v. 93, p. 4249–4257, doi:10.1029/JB093iB05p04249.

Zandt, G., Leidig, M., Chmielowski, J., Baumont, D., and Yuan, X., 2003a, Seismic Detection and Characterization of the Altiplano-Puna Magma Body, Central Andes: pure and applied geophysics, v. 160, p. 789–807, doi:10.1007/PL00012557.

Zandt, G., Leidig, M., Chmielowski, J., Baumont, D., and Yuan, X., 2003b, Seismic Detection and Characterization of the Altiplano-Puna Magma Body, Central Andes: pure and applied geophysics, v. 160, p. 789–807, doi:10.1007/PL00012557.

Chapter 3: Measuring diffuse helium flux from Sulphur Springs, New Mexico

3.1 Introduction

3.1.1 Diffuse helium degassing

Gases emitted from volcanic systems provide valuable insights into processes occurring beneath the surface and potential volcanic activity in the future (Fischer and Chiodini, 2015). These gases can either be visible, typically from fumaroles, solfataras, and plumes, or invisible, in the form of diffuse degassing (Alonso et al., 2022). Understanding this diffuse (or passive) degassing is important because it is estimated to account for 90-99% of the total volatiles emitted from volcanoes worldwide (Fischer and Chiodini, 2015). Emissions from volcanic systems are dominated by water and CO_2 which leads to the focus of degassing studies in volcanic environments on CO_2 (Padrón et al., 2012, 2013; Fischer and Chiodini, 2015). As magma derived gas rises towards the surface, it is subject to scrubbing processes that can strongly affect the composition of the gas when it is emitted at the surface, either though gas-rock interactions or by fractionation (Federico et al., 2002; Tassi et al., 2007; L. Marini and B. Gambardella, 2009; Padrón et al., 2013). This dilution can result in changes in the gas composition, shifts in gas fluxes between the magma at depth and at the surface, and it can impact the gas emissions observed prior to volcanic eruptions (Symonds et al., 2001; Padrón et al., 2013; Alonso et al., 2021). However, helium is a noble gas whose geochemical properties (highly mobile, chemically inert, radioactively stable, non-biogenic,

and relatively insoluble in water) reduce these scrubbing effects and chemical interactions as it travels towards the surface (Padrón et al., 2013; Rodríguez et al., 2015; Alonso et al., 2021). Because of this, helium is considered an excellent geochemical tracer that can be used to determine what is occurring at depth (Padrón et al., 2012; Alonso et al., 2021).

Helium has two naturally occurring isotopes: ^{3}He and ^{4}He (Fischer and Chiodini, 2015; Alonso et al., 2022). ^{4}He is an alpha particle produced by radioactive decay of ^{238}U, ^{235}U, and ^{232}Th, which are primarily concentrated in the Earth's crust (Ballentine and Burnard, 2002; Rodríguez et al., 2015; Boucher et al., 2018). On the other hand, ^{3}He is primordial and is generated by mantle degassing (Graham, 2002; Rodríguez et al., 2015). ^{4}He is much more abundant than ^{3}He, as evidenced by the atmospheric $^{3}He/^{4}He$ ratio (RA) of $1.39x10^{-6}$ (Graham, 2002). However, in active volcanic regions, the $^{3}He/^{4}He$ ratio is much higher, which points towards ongoing ^{3}He emission from Earth's interior (Allard, 1992). Thus, understanding and quantifying helium emissions from volcanic regions is vital for evaluating current mantle degassing.

Helium emissions have been used in a variety of different ways: as precursors to volcanic unrest (Padrón et al., 2013), for locating areas with potential geothermal resources (Rodríguez et al., 2015; Alonso et al., 2022), identifying active fracture or fault systems (Padrón et al., 2012), and tracing degassing of magmatic bodies (Boucher et al., 2018; Alonso et al., 2021). Additionally, knowing the He flux leads to being able to calculate other volatile fluxes, such as CO_2, SO_2, H_2S, etc, using the ratio of the volcanic gas to He (Hilton et al., 2002). Two separate methods have been used to determine the He flux at arc volcanoes. In the first, magma production rate of arcs is assumed to be 20% of the mid-ocean

ridge and this is combined with an estimate of the helium degassing flux for the mid-ocean ridge (Crisp, 1984; Hilton et al., 2002). This allows a determination of the arc ^{3}He flux assuming that the ^{3}He content in the magma is consistent between the mantle wedge and beneath the spreading zones (Hilton et al., 2002). The second method uses the total ^{3}He flux for subaerial volcanism and then estimates the amount that would be derived specifically from arc volcanoes (Hilton et al., 2002).

For example, Allard et al. (1992) determined the global He flux by steady volcanic plume emissions was 240-310 mol/year and approximately 70 mol/year was arc-related. This was done by combining $^{3}He/CO_2$ molar ratios with estimates of CO_2 flux from arc and non-arc volcanoes (Allard, 1992). If the CO_2 flux and the $^{3}He/CO_2$ ratio are known for a specific volcano, then the ^{3}He flux can be calculated. At Teide volcano, Tenerife, Canary Islands, based on the $^{3}He/CO_2$ ratio and the CO_2 flux, the ^{3}He flux was determined to be 0.052 mol/year (Hernández et al., 1998).

A more direct method for determining the helium flux uses Fick's law to calculate the diffusive helium flux (Etiope and Martinelli, 2002; Padrón et al., 2013). This method was used to show the increased helium emissions immediately preceding the 2011-2012 submarine eruption off the coast of El Heirro Island, Canary Islands, Spain (Padrón et al., 2013). In this discussion, the diffusive helium flux for Sulphur Springs in the Jemez Mountains, New Mexico was determined using the process described by Padrón et al. (2013).

3.1.2 Valles Caldera

Running from east-central Arizona to southeastern Colorado is a chain of volcanic features known as the Jemez Lineament (Trainer et al., 2000). In north-central New Mexico, the Jemez Lineament intersects with the Rio Grande Rift and this is the location of the Jemez volcanic field, which began forming approximately 13 Ma (Self et al., 1986; Trainer et al., 2000). The Jemez volcanic field was caused by two caldera-forming eruptions: the first occurred 1.47 Ma and formed the Toledo Caldera, while the second occurred at 1.12 Ma and wiped out the Toledo Caldera, replacing it with the Valles Caldera (Trainer et al., 2000). This eruption deposited approximately 250 km^3 of rhyolitic ignimbrite and 15 km^3 of Plinian fall deposits which are known as the upper Bandelier Tuff (Phillips et al., 2007). Following this caldera-forming eruption, a resurgent dome (Redondo Peak) formed in the center of the caldera accompanied by smaller eruptions between 1 Ma and 0.13 Ma (Goff and Gardner, 1994; Phillips et al., 2007).

Underneath the central and western portions of the Valles Caldera is a geothermal system that had been considered in the past as a potential source of geothermal energy (Goldstein et al., 1982). Two types of thermal waters are discharged from the Valles Caldera: thermal meteoric water and acid sulfate water (Trainer et al., 2000). The thermal meteoric water chemically and isotopically resembles cold groundwater that is circulating in the upper 1,500 ft of the caldera, heated by the high heat flux in the area (Vuataz and Goff, 1986; Trainer et al., 2000). The acid sulfate water is primarily found on the western slope of the resurgent dome, coming from fractures and faults (Trainer et al., 2000). The largest concentration of acid sulfate springs occur in the Sulphur Springs area, which also contains

numerous thermal and nonthermal springs, mudpots, fumaroles, and sublime sulphur (Trainer et al., 2000).

3.1.3 Sulphur Springs hydrothermal system

The Valles Caldera geothermal system has been investigated as a potential source of geothermal energy (Goldstein et al., 1982; Goff et al., 1992; Trainer et al., 2000). In the early 1960s, four exploratory wells were drilled in the Sulphur Creek area and over the next three decades, further research into the geothermal potential of the system was carried out (Goldstein et al., 1982; Trainer et al., 2000). Much of the current knowledge of the geologic, geophysical, and hydrologic properties of the Valles Caldera hydrothermal system comes from those early investigations.

The area of the entire geothermal system is approximately 12-15 square miles and the temperature ranges from 225 to 330 °C, depending on the depth (Trainer et al., 2000). The Valles Caldera hydrothermal system contains two subsystems: the Redondo Creek reservoir and the Sulphur Springs reservoir (Goff et al., 1992; Trainer et al., 2000). Most of the previous studies focused on the Redondo Creek area because it showed the greatest potential for geothermal development, but the Sulphur Springs subsystem is the focus of this discussion (Figure 3.1). These two reservoirs appear to be separated from each other, suggested by the chemical and isotopic composition of waters from the areas (Trainer et al., 2000). In the Sulphur Springs reservoir, there is a liquid dominated zone composed of stacked hydrothermal aquifers underlying a vapor dominated zone and the two zones are separated by approximately 800 ft of sealed caldera-fill rocks (Trainer et al., 2000). While

dating of spring deposits and core samples shows that the hydrothermal system has been active for 1 Ma, this vapor zone only formed about 0.5 Ma (Goff et al., 1992). Most of the water in the hydrothermal system has a meteoric origin, but some samples from deeper depths have elevated $^{3}He/^{4}He$ ratios, which indicates a potential mantle or magmatic component (Goff et al., 1992).

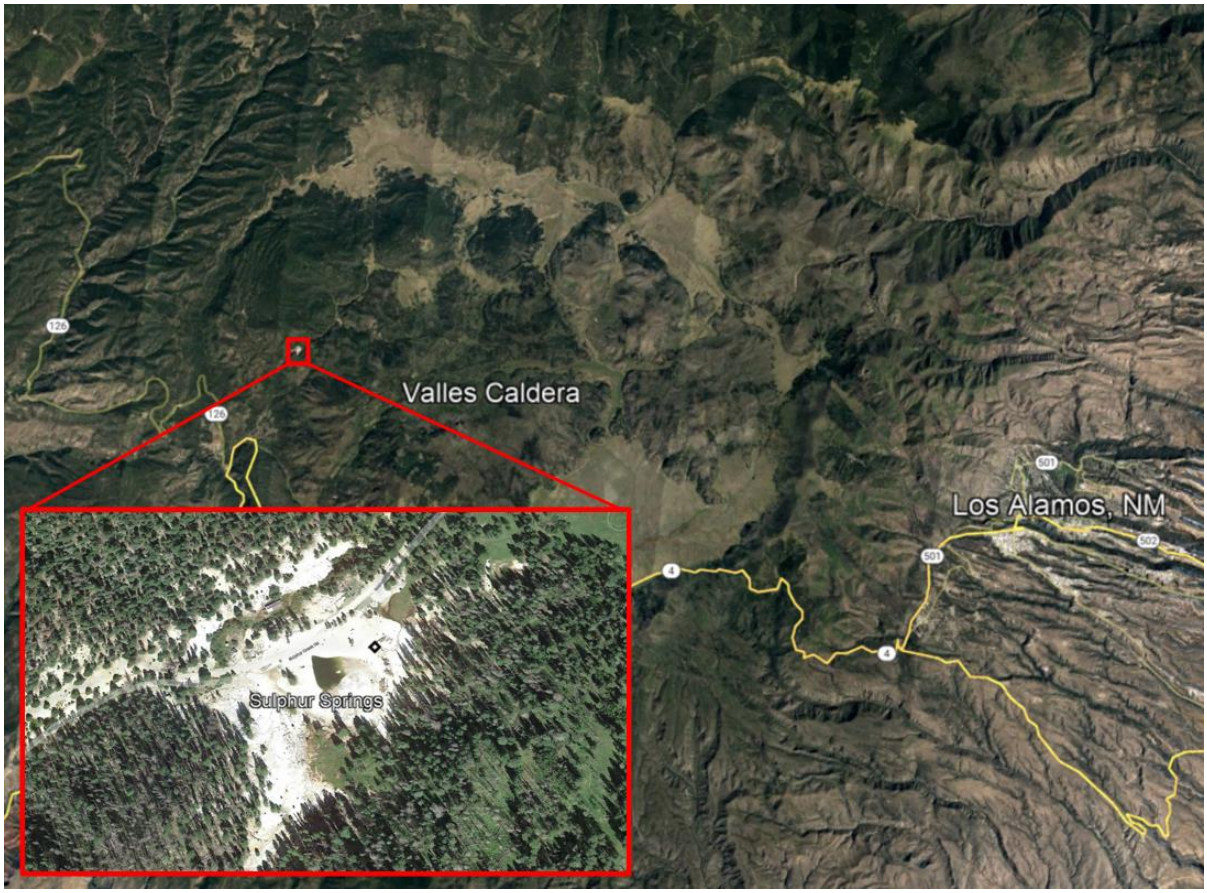

Figure 3.1: Location of Valles Caldera in relation to the nearby town of Los Alamos, New Mexico. Inset shows the exact location of Sulphur Springs and the black diamond represents the Footbath Spring.

3.1.4 Sources for helium in Sulphur Springs

Most of the gases in the Sulphur Springs hydrothermal system likely originate from the atmosphere, thermal metamorphism of underlying carbonate rocks, or from chemical reactions in the reservoir (Truesdell and Janik, 1986). However, helium is the exception to this and enrichments of ^{3}He in the hydrothermal fluids suggest a mantle derived helium component, possibly pointing towards the presence of a magmatic source (Smith and Kennedy, 1985; Goff et al., 1992; Goff and Gardner, 1994; Trainer et al., 2000). The $^{3}He/^{4}He$ ratios for the Sulphur Springs area are 3.9-4.8, significantly higher than typical crustal gases dominated by radiogenic helium (~0.01-0.1) (Smith and Kennedy, 1985). Mantle derived helium from arc volcanoes and MORBs are usually >6 R/R_a, with the highest values associated with hot spots such as Hawaii, Iceland, or Yellowstone (Smith and Kennedy, 1985; Graham, 2002). The intermediate values at Sulphur Springs may indicate mixing between mantle helium and crustal radiogenic helium (Smith and Kennedy, 1985).

The goal of this study is to use Fick's Law to calculate a diffuse helium flux for the Sulphur Springs area in the Valles Caldera, New Mexico. Extensive CO_2 flux surveys have been conducted there previously (Smith, 2016; Rahilly, 2020), but the helium flux is still unknown. This helium flux will then be compared to other volcanic systems in order to understand how the Sulphur Springs site fits into the larger picture. This method for determining helium flux is widely applicable and could be applied to other volcanic systems, such as Uturuncu in Bolivia.

3.2 Methods

3.2.1 Diffusive helium flux

Fick's Law was used to determine the diffusive helium flux (F_D) (Etiope and Martinelli, 2002).

$$\text{Equation 3.1: } F_D = D_e \left(\frac{dC}{dz}\right),$$

where D_e is the global diffusion coefficient (m^2/s) and dC (kg/m^3) is the variation of the gas concentration along the depth dz (m). The global diffusion coefficient is n^2D_m, where n is the effective porosity (%) and D_m is the diffusion coefficient of helium in air. D_m is $0.7x10^{-4}$ m^2/s at 25 °C as found by Pandey et al., 1974. Soil gas samples from the Footbath Spring in Sulphur Springs in the Jemez Mountains, NM were used to determine the helium concentration of the soil (Figure 3.1). A soil sample was also collected in order to calculate the porosity of the soil.

Equation 3.1 uses the effective porosity of the soil which is the interconnected pore space that allows fluid to flow through the material (Woessner and Poeter, 2021). Typically, effective porosity is equal to or less than the total porosity of the soil and for uncemented, granular material, the total porosity can be assumed to be the same as the effective porosity (Woessner and Poeter, 2021). The surface material at Sulfur Springs is primarily unconsolidated, course-grained, altered Bandelier Tuff. Because of this, the effective porosity was assumed to be equal to the total porosity, so total porosity was substituted for effective porosity in Equation 3.1.

3.2.2 Soil gas sample collection & analysis

Soil gas samples were collected at 35° 54’ 28.89’’ N, -106° 36’ 56.47’’ W near the Footbath Spring (Figure 3.1). A hollow, stainless-steel pipe was pushed 40 cm into the ground and care was taken to ensure that the base of the pipe was not blocked by soil or rocks and that it experienced unrestricted gas flow. Four soil gas samples were collected using evacuated Giggenbach bottles, three at 40 cm depth and one at the surface (Figure 3.2). Gas analyses were performed in the Volatiles Laboratory at the University of New Mexico using a Pfeiffer Quadrupole Mass Spectrometer (QMS).

Figure 3.2: Using a syringe to collect a soil gas sample at a depth of 40 cm.

3.2.3 Soil sample collection & analysis

The following is the equation used to determine the porosity (η) of the soil sample.

Equation 3.2: $\eta = \left. \frac{V_t - M_s}{G_s * \rho_w} \right/ V_t$

V_t is the total volume of the soil mass, M_s is the mass of the dry soil solids, G_s is the specific gravity, and ρ_w is the density of water (1 g/cm^3). In order to determine these values, a soil sample was collected from approximately the same location as the soil gas samples.

Determining the total volume of a soil mass can be challenging, especially if the soil is unconsolidated, which is the case for Sulfur Springs. For this location, the sand cone method was used as an indirect method to calculate the volume of the soil mass by measuring the volume of the hole from which the sample was removed (Bowles, 2001). By using a sand with a known, constant density, the volume of the hole can be calculated by weighing the amount of sand that fills the hole. Ottawa sand has a density of 2.65 g/cm^3 and was used for this measurement (El Ghoraiby et al., 2020).

First, a hole large enough for a 29x29 cm metal plate to lay flat at the base of the hole was dug to a depth of 40 cm. The opening in the center of the metal plate was used to excavate a small hole beneath the plate. All of the soil removed from the small hole was stored in a plastic bag for later weighing and analysis in the lab. The volume of the hole where the soil was removed was determined using the sand cone method (Bowles, 2001). The sand cone device, consisting of a plastic jug filled with Ottawa sand attached to a valve and funnel, was placed over the opening in the metal plate so that the funnel was facing downwards (Figure 3.3). The valve was opened so that sand flowed into the hole until it filled up the hole and the funnel. After closing the valve, the remaining sand in the container

was placed to the side to be weighed later in order to calculate the mass of sand that filled the hole.

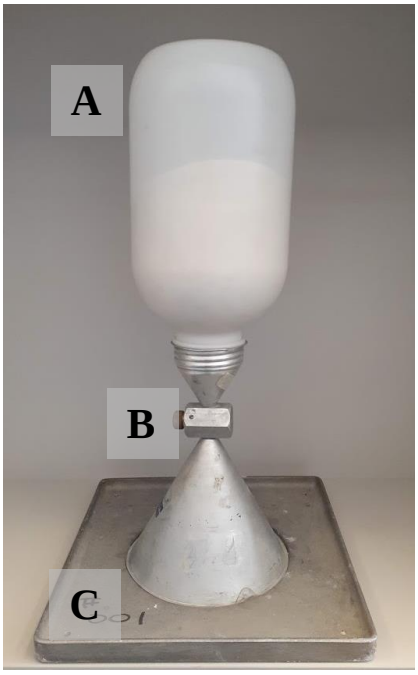

Figure 3.3: A) Plastic container filled with Ottowa sand, B) valve and funnel, C) metal plate with circular cutout for the sand cone device to be placed in, as pictured above.

Immediately after returning from the field, the soil sample was weighed and found to be 681.82 g. This includes the mass of moisture in the sample, so the soil was placed in a drying oven for 24 hours at 110 ± 5 °C. The dry sample mass (M_s) after removal from the oven was 519.10 g. Additionally, the mass of the sand in the hole (M_{sand}) was 635.67 g. The total volume of the soil mass (V_t) which is the same as the volume of the hole was 239.88 cm^3 and was calculated by dividing M_{sand} by the Ottawa sand density (ρ_s).

The final piece of information required for calculating the soil porosity is the specific gravity (G_s) of the soil sample. The soil sample was split into four smaller samples and

weighed. Four 250 mL volumetric flasks were filled with water to a mark on the neck and weighed (Table 2). The water temperature was approximately 20 °C. Then half of the water was removed and the soil samples were poured into the flasks. For sample 1 and 4, water was slowly added to the mixture until the flask was filled up to the mark. For sample 2 and 3, the flask was attached to a vacuum for 15 minutes to remove air bubbles from the samples before filling the rest of the flask with water (Figure 3.4).

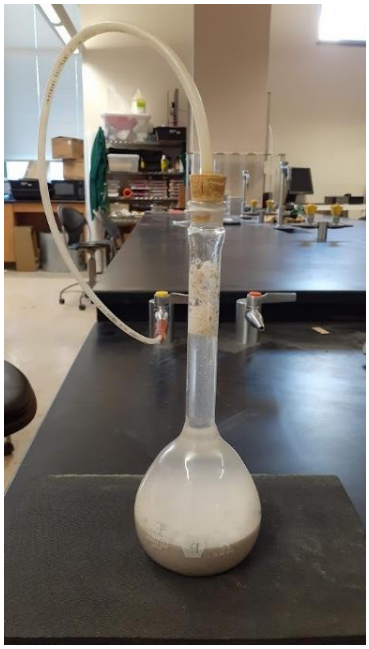

Figure 3.4: A volumetric flask filled with the soil sample and connected to a vacuum in order to remove air bubbles from the sample.

Air present in the sample decreases the mass of the flask + soil + water filled to the mark (M_{bws}) and results in a lower G_s value (Bowles, 2001). Removing air from the sample provides a more accurate value for G_s, so the average of the G_s for samples 2 and 3 was used as the specific gravity in the final porosity calculation. After each flask was weighed, the

soil-water mixture was poured into pans and dried in an oven overnight and weighed the next morning (M_{ds}). The following equation was used to calculate the specific gravity of the soil sample:

$$\text{Equation 3.3: } G_s = \frac{M_{ds}}{M_{bw}+M_{ds}-M_{bws}},$$

where M_{ds} is the mass of dry soil, M_{bw} is the mass of the flask + water to the mark, and M_{bws} is the mass of the flask + soil + water filled to the mark.

3.3 Results

3.3.1 Soil gas samples

One of the soil gas samples was disregarded because of an error with the results, possibly caused by a faulty seal on the Giggenbach bottle. The helium concentrations for the remaining three samples are shown in Table 3.1. Samples 1 and 2 are representative of the helium concentrations at a depth of 40 cm and sample 3 is the helium concentration at the surface. The difference between the surface concentration and the concentration at 40 cm depth serves as the dC value in Equation 3.1. The two dC values were 175.52 ppm and 483.68 ppm.

Table 3.1: Helium concentrations for soil gas samples.

Sample	**Collection depth**	**He (ppm)**
1	40 cm	193.46
2	40 cm	501.62
3	Surface	17.944

3.3.2 Soil samples

Samples 2 and 3 in Table 3.2 were considered the more accurate measurements because a vacuum was used to remove air from the samples. The average of these two G_s values (2.3935) was used in the final porosity calculation. Table 3.3 shows all of the parameters required for calculating the porosity of the soil sample. The porosity for Sulphur Springs was 9.5% calculated using Equation 3.2.

Table 3.2: Data for determining the specific gravity of the soil sample.

Sample	**M_{ds} (g)**	**M_{bw} (g)**	**M_{bws} (g)**	**G_s**
1	83.3	345.8	390.9	2.181
2	84.8	345.2	394.1	2.362
3	87.8	356.5	408.1	2.425
4	87.0	356.4	403.4	2.175

Table 3.3: Data used to calculate the porosity of the soil sample.

Wet sample	681.82 g
Dry sample (M_s)	519.10 g
Specific gravity (G_s)	2.3935
Mass of sand in hole (M_{sand})	635.67 g
Density of Ottowa sand (ρ_s)	2.65 g/cm^3
Total volume of soil mass (V_t)	239.88 cm^3
Density of water (ρ_w)	1 g/cm^3

3.3.3 Helium flux

With the above information, the He flux for the Footbath Spring was calculated using Equation 3.1. The resulting He flux values were 0.0108 g/m^2/day and 0.00392 g/m^2/day. The Sulphur Springs area was estimated to be 43,153 m^2 and the He emission was assumed to be

constant across the entire degassing area. Using this area, the total He emissions from Sulphur Springs is between 169 and 466 g/day or 0.068-0.187 tons/year.

3.4 Discussion

3.4.1 Sulphur Springs porosity measurements

The value of 9.5% with a dry bulk density of 2.164 g/cm^3 for the Sulphur Springs porosity is towards the lower end of previous porosity measurements in the late 1980s (Figure 3.5).

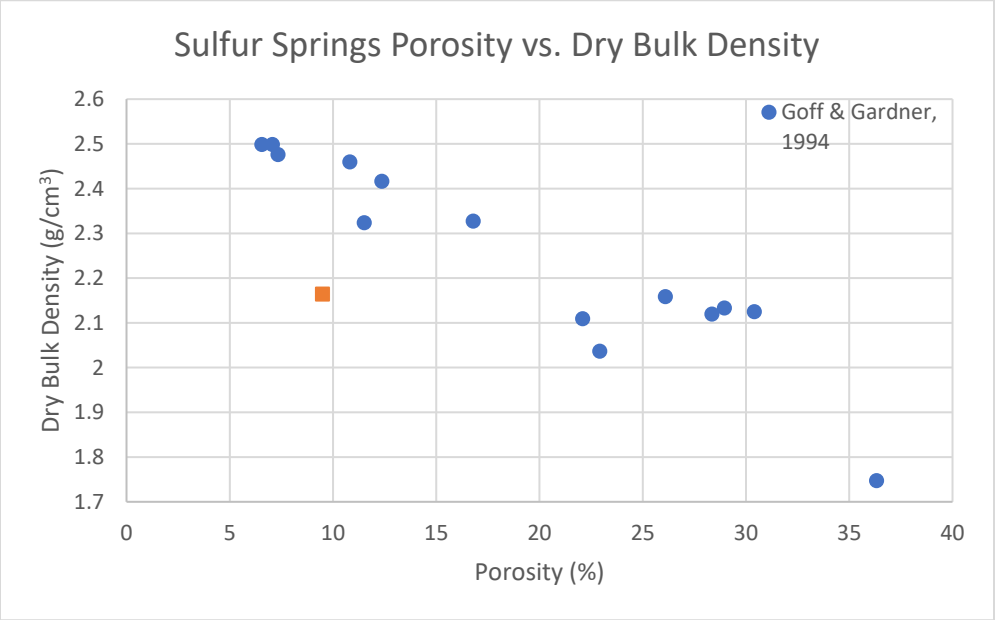

Figure 3.5: Sulphur Springs porosity compared to data from Goff & Gardner, 1994.

Comparing the 2021 porosity measurements to the 1980 measurements is challenging because the older values were based on core samples from deep drill holes. Hole VC-2A was located in the Sulphur Springs area and reached a depth of 528 m and hole VC-2B, about 0.5

km east of Sulphur Springs was drilled to 1762 m (Goff and Gardner, 1994). Generally, porosities for the caldera-fill sequence from these holes were between 10-30% with dry bulk densities ranging from 1.74 to 2.50 g/cm^3 (Goff and Gardner, 1994). Variation between the 1980s values and the 2021 values is likely a result of different sampling locations (at depth vs. the surface), type of sample (core sample vs. soil sample), and the almost 30-year time period between sampling. However, this comparison demonstrates that a porosity value of 9.5% is not outside of the range of previous accepted porosity measurements.

3.4.2 CO_2 flux from He flux and CO_2/He ratio

The helium flux (this study) and CO_2/He ratio (Siluk & Fischer, unpublished results) for the Footbath Spring in Sulphur Springs can be used to calculate the expected CO_2 flux from the spring. Previous surveys of the Sulphur Springs area constrain the actual CO_2 flux and provide a way to validate the methods used in this study for determining the helium flux (Rahilly, 2020). Based on measurements of diffuse CO_2 flux between 2016 and 2019, Footbath Spring has highly elevated CO_2 emissions, with the highest values between 11776-61455 g/m^2/day (Rahilly, 2020). CO_2 fluxes calculated based on the helium flux and CO_2/He ratio range from 2,017 to 26,110 g/m^2/day. The measured and the calculated CO_2 flux fall within a similar range, indicating that the helium flux is valid for this area.

3.4.3 Comparison of Sulphur Springs He flux to other volcanic systems

Helium flux has been measured in various volcanic systems around the globe. Table 3.4 highlights some of these measurements and shows how the helium flux at Sulphur Springs fits into the wider picture.

Table 3.4: Helium flux in tons/year for Sulphur Springs, New Mexico and various other volcanic systems.

Location	Helium flux (tons/year)	Reference
Sulphur Springs, New Mexico	0.068-0.187	This paper
El Heirro Island, Canary Islands	3.62 ± 0.4	Padrón et al., 2013
Cumbre Vieja, La Palma Island, Canary Islands	7.24-15.29	Padrón et al., 2012
Heart Lake Geyser Basin, Yellowstone	0.0304	Lowenstern et al., 2014
Wakamiko Caldera, Japan	0.0043	Roulleau et al., 2013

Of the helium fluxes reported in Table 4, the highest comes from the active volcano on La Palma Island, Cumbre Vieja, and reaches a maximum value of 15.29 tons/year. The lowest flux is 0.0043 tons/year at Wakamiko Caldera, an active submarine crater in north-eastern Kagoshima Bay, Japan. Helium flux from Sulphur Springs, New Mexico falls towards the lower end of this range, with a max value of 0.187 tons/year. The elevated values at Cumbre Vieja are likely a result of N-S and N-W running rifts on the island that create zones of increased permeability (Padrón et al., 2012). These routes for preferential degassing allow the helium to rapidly rise and degas at the surface, leading to its increased helium emissions (Padrón et al., 2012). The lower values measured at measured at Sulphur Springs may be a result of fewer available paths for the helium to reach the surface. Additionally, there are distinct differences between these two volcanic systems that likely lead to variations in the helium emissions. Primarily, Cumbre Veija is the most active volcano in the Canary Islands and most recently erupted in September of 2021, while Valles Caldera has geothermally active regions but has not actively erupted since 0.13 Ma (Goff and Gardner, 1994; Phillips

et al., 2007; Carracedo et al., 2022). Understanding the helium emissions at various volcanic systems allows for a better knowledge of the underlying geology and processes.

3.5 Conclusions

The vast majority of volatile emissions from volcanic systems are in the form of water and CO_2, which naturally leads to many studies focusing on these gases. However, helium can be a powerful geochemical tracer and understanding these emissions can lead to interpreting processes occurring at depth. As an example, diffusive helium flux increased significantly prior to a submarine eruption off the coast of El Heirro Island, Canary Islands indicating that helium emission can potentially be used as a precursor to volcanic activity (Padrón et al., 2013). While several extensive CO_2 surveys have been conducted at Sulphur Springs in the Jemez Mountains (Rahilly, 2020), an estimate of the helium flux had not occurred before this discussion. Using Fick's Law and samples from the Footbath Spring, the total helium flux from Sulphur Springs was estimated to be 0.068-0.187 tons/year.

This discussion showcases the methods for determining the diffusive helium flux from a volcanic system and can potentially be applied to a variety of other areas, such as Uturuncu in Bolivia. Estimating the helium emissions can help constrain these systems and lead to an increased understanding of the subsurface processes.

Acknowledgements

This work was supported by the Volatiles Laboratory in the Earth and Planetary Sciences Department. Special thanks to John Stormont of the Civil, Construction, and

Environmental Engineering department at the University of New Mexico for assistance with calculating soil porosity.

References

Allard, P., 1992, Global emissions of helium-3 by subaerial volcanism: Geophysical Research Letters, v. 19, p. 1479–1481, doi:10.1029/92GL00974.

Alonso, M. et al., 2021, Changes in the thermal energy and the diffuse 3He and 4He degassing prior to the 2014–2015 eruption of Pico do Fogo volcano, Cape Verde: Journal of Volcanology and Geothermal Research, v. 416, p. 107271, doi:10.1016/j.jvolgeores.2021.107271.

Alonso, M. et al., 2022, Thermal energy and diffuse 4He and 3He degassing released in volcanic-geothermal systems: Renewable Energy, v. 182, p. 17–31, doi:10.1016/j.renene.2021.10.016.

Ballentine, C.J., and Burnard, P.G., 2002, Production, Release and Transport of Noble Gases in the Continental Crust: Reviews in Mineralogy and Geochemistry, v. 47, p. 481–538, doi:10.2138/rmg.2002.47.12.

Boucher, C., Lan, T., Marty, B., Burnard, P.G., Fischer, T.P., Ayalew, D., Mabry, J., Maarten de Moor, J., Zelenski, M.E., and Zimmermann, L., 2018, Atmospheric helium isotope composition as a tracer of volcanic emissions: A case study of Erta Ale volcano, Ethiopia: Chemical Geology, v. 480, p. 3–11, doi:10.1016/j.chemgeo.2017.05.011.

Bowles, J., 2001, Engineering Properties of Soils and their Measurement: McGraw-Hill Companies.

Carracedo, J.C. et al., 2022, The 2021 eruption of the Cumbre Vieja Volcanic Ridge on La Palma, Canary Islands:, https://eartharxiv.org/repository/view/3105/ (accessed May 2022).

Crisp, J.A., 1984, Rates of magma emplacement and volcanic output: Journal of Volcanology and Geothermal Research, v. 20, p. 177–211, doi:10.1016/0377-0273(84)90039-8.

El Ghoraiby, M., Park, H., and Manzari, M.T., 2020, Physical and Mechanical Properties of Ottawa F65 Sand, *in* Kutter, B.L., Manzari, M.T., and Zeghal, M. eds., Model Tests and Numerical Simulations of Liquefaction and Lateral Spreading, Cham, Springer International Publishing, p. 45–67, doi:10.1007/978-3-030-22818-7_3.

Etiope, G., and Martinelli, G., 2002, Migration of carrier and trace gases in the geosphere: an overview: Physics of the Earth and Planetary Interiors, v. 129, p. 185–204, doi:10.1016/S0031-9201(01)00292-8.

Federico, C., Aiuppa, A., Allard, P., Bellomo, S., Jean-Baptiste, P., Parello, F., and Valenza, M., 2002, Magma-derived gas influx and water-rock interactions in the volcanic

aquifer of Mt. Vesuvius, Italy: Geochimica et Cosmochimica Acta, v. 66, p. 963–981, doi:10.1016/S0016-7037(01)00813-4.

Fischer, T.P., and Chiodini, G., 2015, Chapter 45 - Volcanic, Magmatic and Hydrothermal Gases, *in* Sigurdsson, H. ed., The Encyclopedia of Volcanoes (Second Edition), Amsterdam, Academic Press, p. 779–797, doi:10.1016/B978-0-12-385938-9.00045-6.

Goff, F., and Gardner, J.N., 1994, Evolution of a mineralized geothermal system, Valles Caldera, New Mexico: Economic Geology, v. 89, p. 1803–1832, doi:10.2113/gsecongeo.89.8.1803.

Goff, F., Gardner, J.N., Hulen, J.B., Nielson, D.L., Charles, R., WoldeGabriel, G., Vuataz, F.-D., Musgrave, J.A., Shevenell, L., and Kennedy, B.M., 1992, The Valles caldera hydrothermal system, past and present, New Mexico, USA: Scientific Drilling, v. 3, p. 181–204.

Goldstein, N.E., Holman, W.R., and Molloy, M.W., 1982, Final report of the Department of Energy Reservoir Definition Review Team for the Baca Geothermal Demonstration Project: Lawrence Berkeley Lab., CA (USA) LBL-14132, doi:10.2172/6764368.

Graham, D.W., 2002, Noble Gas Isotope Geochemistry of Mid-Ocean Ridge and Ocean Island Basalts: Characterization of Mantle Source Reservoirs: Reviews in Mineralogy and Geochemistry, v. 47, p. 247–317, doi:10.2138/rmg.2002.47.8.

Hernández, P.A., Pérez, N.M., Salazar, J.M., Nakai, S., Notsu, K., and Wakita, H., 1998, Diffuse emission of carbon dioxide, methane, and helium-3 from Teide Volcano, Tenerife, Canary Islands: Geophysical Research Letters, v. 25, p. 3311–3314, doi:10.1029/98GL02561.

Hilton, D., Fischer, T., and Marty, B., 2002, Noble Gases and Volatile Recycling at Subduction Zones: Reviews in Mineralogy & Geochemistry - REV MINERAL GEOCHEM, v. 47, p. 319–370, doi:10.2138/rmg.2002.47.9.

L. Marini and B. Gambardella, 2009, Geochemical modeling of magmatic gas scrubbing: Annals of Geophysics, v. 48, doi:10.4401/ag-3230.

Lowenstern, J.B., Evans, W.C., Bergfeld, D., and Hunt, A.G., 2014, Prodigious degassing of a billion years of accumulated radiogenic helium at Yellowstone: Nature, v. 506, p. 355–358, doi:10.1038/nature12992.

Padrón, E. et al., 2013, Diffusive helium emissions as a precursory sign of volcanic unrest: Geology, v. 41, p. 539–542, doi:10.1130/G34027.1.

Padrón, E., Pérez, N.M., Hernández, P.A., Sumino, H., Melián, G., Barrancos, J., Nolasco, D., and Padilla, G., 2012, Helium emission at Cumbre Vieja volcano, La Palma,

Canary Islands: Chemical Geology, v. 312–313, p. 138–147, doi:10.1016/j.chemgeo.2012.04.018.

Phillips, E.H., Goff, F., Kyle, P.R., McIntosh, W.C., Dunbar, N.W., and Gardner, J.N., 2007, The 40Ar/39Ar age constraints on the duration of resurgence at the Valles caldera, New Mexico: Journal of Geophysical Research: Solid Earth, v. 112, doi:10.1029/2006JB004511.

Rahilly, K.E., 2020, Diffuse Flux and Carbon Isotope Composition of Carbon Dioxide Emitted from Valles Caldera, Yellowstone Caldera, and Southwestern Utah Geothermal Sites:

Rodríguez, F. et al., 2015, Diffuse Helium and Hydrogen Degassing to Reveal Hidden Geothermal Resources in Oceanic Volcanic Islands: The Canarian Archipelago Case Study: Surveys in Geophysics, v. 36, p. 351–369, doi:10.1007/s10712-015-9320-8.

Roulleau, E., Sano, Y., Takahata, N., Kawagucci, S., and Takahashi, H., 2013, He, N and C isotopes and fluxes in Aira caldera: Comparative study of hydrothermal activity in Sakurajima volcano and Wakamiko crater, Kyushu, Japan: Journal of Volcanology and Geothermal Research, v. 258, p. 163–175, doi:10.1016/j.jvolgeores.2013.04.003.

Self, S., Goff, F., Gardner, J.N., Wright, J.V., and Kite, W.M., 1986, Explosive rhyolitic volcanism in the Jemez Mountains: Vent locations, caldera development and relation to regional structure: Journal of Geophysical Research: Solid Earth, v. 91, p. 1779–1798, doi:10.1029/JB091iB02p01779.

Smith, J., 2016, CO2 Flux Along Faults of the Central Rio Grande Rift, New Mexico:

Smith, S.P., and Kennedy, B.M., 1985, Noble gas evidence for two fluids in the Baca (Valles Caldera) geothermal reservoir: Geochimica et Cosmochimica Acta, v. 49, p. 893–902.

Symonds, R.B., Gerlach, T.M., and Reed, M.H., 2001, Magmatic gas scrubbing: implications for volcano monitoring: Journal of Volcanology and Geothermal Research, v. 108, p. 303–341, doi:10.1016/S0377-0273(00)00292-4.

Tassi, F., Vaselli, O., Capaccioni, B., Montegrossi, G., Barahona, F., and Caprai, A., 2007, Scrubbing process and chemical equilibria controlling the composition of light hydrocarbons in natural gas discharges: An example from the geothermal fields of El Salvador: Geochemistry, Geophysics, Geosystems, v. 8, doi:10.1029/2006GC001487.

Trainer, F.W., Rogers, R.J., and Sorey, M.L., 2000, Geothermal hydrology of Valles caldera and the southwestern Jemez Mountains: U.S Geological Survey Water-Resources Investigations Report 00–4067.

Truesdell, A.H., and Janik, C.J., 1986, Reservoir processes and fluid origins in the Baca geothermal system, Valles Caldera, New Mexico (USA).: Journal of Geophysical Research, v. 91, p. 17.

Vuataz, F.-D., and Goff, F., 1986, Isotope geochemistry of thermal and nonthermal waters in the Valles Caldera, Jemez Mountains, northern New Mexico (USA).: Journal of Geophysical Research, v. 91, p. 1835–1854, doi:10.1029/JB091iB02p01835.

Woessner, W., and Poeter, E., 2021, Hydrogeologic Properties of Earth Materials and Principles of Groundwater Flow: The Groundwater Project, 205 p.

Chapter 4: Mapping CO_2 emissions from the Kīlauea Caldera, Hawaii

4.1 Introduction

4.1.1 Kīlauea's eruptive history

A chain of volcanoes and seamounts, known as the Hawaiian Islands, stretches 6000 km across the Pacific Ocean (Poland et al., 2012, 2014). It was formed as the Pacific Plate drifted over a hotspot in the mantle, resulting in volcanic activity for at least the past 70 million years (Poland et al., 2014). Because of this plate movement, the age of the volcanoes gradually increases towards the northwest (Poland et al., 2012). The island of Hawai'i contains the majority of the active volcanoes in the island chain. Most notable is Kīlauea which is located on the south flank of Mauna Loa and whose historical eruption record extends over 230 years (Wright and Klein, 2014). Like most volcanoes located above hotspots, Kīlauea typically has nonviolent eruptions of basaltic magma, making it an ideal volcano to study (Tilling and Dvorak, 1993).

In 1912, the Hawaiian Volcano Observatory (HVO) was founded, which has kept detailed records of Kīlauea's eruptive history (Wright and Klein, 2014). Prior to the founding of HVO, written and oral records from native Hawaiians and European explorers was the only source of information about the eruptive history at Kīlauea (Wright and Klein, 2014). Kīlauea's notable features include the pit caldera, Halema'uma'u, located within Kīlauea's summit caldera, and the two rift zones that extend from the central caldera, the East rift zone

and the Southwest rift zone (Figure 4.1). Most of Kīlauea's eruptions occur either at the summit or somewhere along the two rift zones (Battaglia et al., 2003). In Kīlauea's history, the East rift zone has been the most active, with eruptions such as the 35 year long Pu'u 'Ō'ō eruption and the devastating 2018 lower East rift zone eruption and summit collapse (Gansecki et al., 2019; Patrick et al., 2019; Kern et al., 2020).

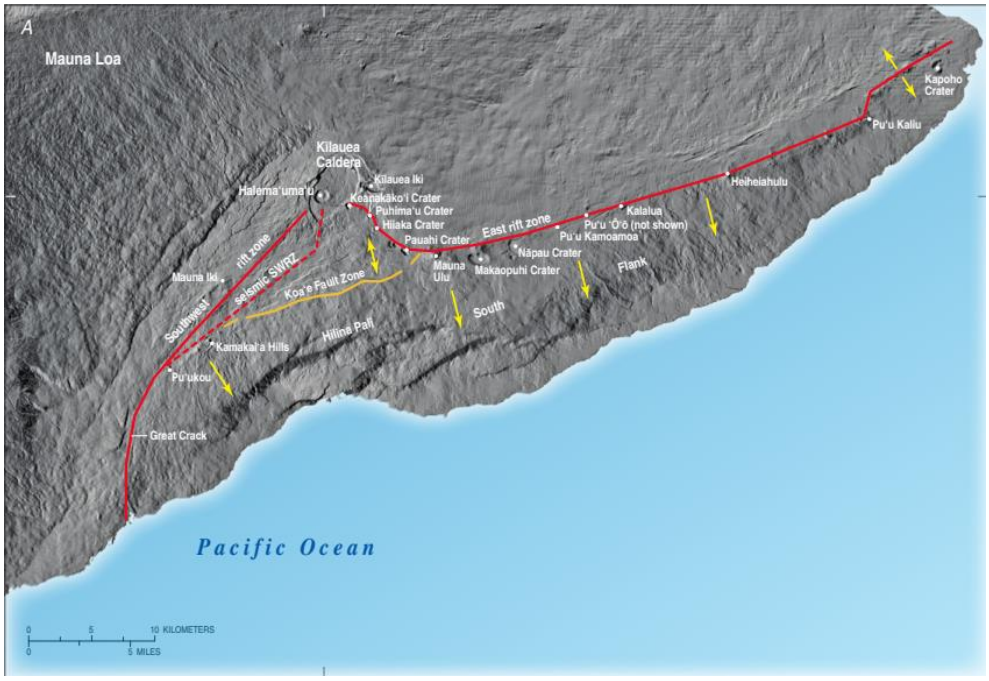

Figure 4.1: Location of Kīlauea's summit caldera and other nearby craters. Kīlauea's two rift zones, the East and the Southwest rift zones, are depicted in red (Wright & Klein, 2014).

4.1.2 Structure beneath Kīlauea

The basic structure of Kīlauea's magmatic system was first proposed in 1960 by Eaton and Murata, who stated that a vertical conduit transported magma from the mantle to a shallow magma reservoir beneath Kīlauea's summit (Eaton and Murata, 1960). As magma flows into this reservoir, pressure builds which eventually leads to either a summit eruption or an intrusion into one of Kīlauea's rift zones (Eaton and Murata, 1960). The transport of

magma into the horizontal pathways beneath the rift zones can either lead to further storage or an eruption far away from Kīlauea's summit (Tilling and Dvorak, 1993). This model has been refined based on geophysical and geochemical monitoring, but has remained largely unchanged over the past several decades (Pietruszka and Garcia, 1999; Poland et al., 2012).

Originally, Kīlauea's magmatic system was viewed as a complex system of dikes and sills located 2-3 km beneath the summit (Fiske and Kinoshita, 1969). However, more recent studies favor a model with two distinct magma reservoirs, primarily located using deformation, gravity, and seismicity studies (Pietruszka and Garcia, 1999; Almendros et al., 2002; Poland et al., 2014; Carey et al., 2015; Pietruszka et al., 2015). The primary magma source beneath the summit is a chamber located approximately 2-4 km under Kīlauea's southern rim (South Caldera reservoir) (Poland et al., 2014; Pietruszka et al., 2015). Numerous seismic, deformation, and gravity studies point towards a second, shallower magma source less than 2 km beneath the eastern rim of the Halemaʻumaʻu pit crater (Halemaʻumaʻu reservoir) (Cervelli and Miklius, 2002; Johnson et al., 2010; Baker and Amelung, 2012; Poland et al., 2014; Carey et al., 2015; Pietruszka et al., 2015). Both of these sources appear to coincide with two major deformation centers located at Kīlauea's summit (Cervelli and Miklius, 2002; Baker and Amelung, 2012; Carey et al., 2015; Pietruszka et al., 2015). Generally, magma in the Kīlauea system passes through the summit magma chamber before either erupting or being transported to one of the rift zones (Hager et al., 2008). Each rift zone has a distinct magma pathway that connects it to either the shallow Halemaʻumaʻu reservoir or the deeper south caldera reservoir (Poland et al., 2014).

4.1.3 Volatiles

Numerous fumaroles, cracks, fractures, and areas of steaming ground throughout the entire summit region emit most of the volatiles (Gerlach et al., 2002). The primary volatile released from Kīlauea is water (H_2O), with lesser amounts of carbon dioxide (CO_2) and sulfur dioxide (SO_2) (Poland et al., 2014). All three allow for the study of different aspects of eruption and intrusion. CO_2 typically degasses as the magma is moving towards shallower depths and the majority has degassed by the time there is an eruption (Wright and Klein, 2014). Magma closer to the surface produces more SO_2, so this volatile provides a way to understand magma movement and whether an eruption is imminent (Poland et al., 2012). Large quantities of water present in the magma increases the pressure in the summit storage reservoir and contributes to eventual eruptions (Wright and Klein, 2014). In this project, the focus was on understanding CO_2 emissions from Kīlauea's summit caldera and how those emissions have changed through time, so the following discussion concentrates on CO_2 and its behavior at Kīlauea.

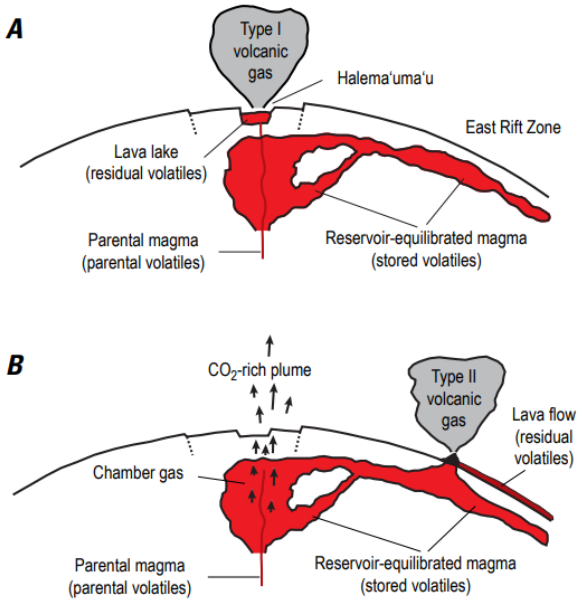

Figure 4.2: A) Type I volcanic gas is relatively undegassed and comes from newly injected magma that is still rich in CO_2, B) Type II volcanic gas comes from degassed magma stored close to the surface, meaning that is depleted in CO_2 (Poland et al., 2014)

There are two endmembers of volcanic gases emitted at Kīlauea that were first identified by Gerlach and Graeber (1985). The type I endmember gas occurs when magma travels directly from depth to the surface and erupts without a long waiting period in the summit magma reservoir (Figure 4.2). The magma is still rich in CO_2 because it has not spent a long time sitting and degassing in the summit magma chamber (Poland et al., 2014). This was the primary gas type present during the 19th century and the beginning of the 20th, when an active lava lake was often present in the Halemaʻumaʻu crater (Gerlach and Graeber, 1985). However, eruptions along Kīlauea's rift zones often occur from magma that has resided in the summit magma reservoir for long time periods and has then been transported many kilometers down the rift zone (Poland et al., 2014). In this case, the magma has had time to degas most of its CO_2 before an eruption occurs (Figure 4.2). Thus, type II volcanic gas is poor in CO_2, but rich in SO_2 and H_2O (Gerlach and Graeber, 1985; Poland et al., 2014).

Modeling indicates that CO_2 primarily exsolves at pressures >10 MPa before the magma has risen to 400 m below the surface, while SO_2 remains dissolved in the melt until the pressure reaches ~2 MPa (<100 m) (Gerlach, 1986). It takes time to degas the CO_2 in a magma, so fresh magma that has not had time to degas in a magma chamber generally has a carbon/sulphur ratio of 2-4 (Tilling and Dvorak, 1993). However, magma sitting at a shallow depth and degassing CO_2 usually has a carbon/sulphur ratio around 0.2-0.3 (Tilling and Dvorak, 1993). Typically, magma erupted from the rift zones has lower carbon/sulphur ratios indicating type II volcanic gas, while magma erupted from the summit caldera can be either type I or type II volcanic gas (Tilling and Dvorak, 1993).

4.1.4 CO_2 emissions from Kīlauea

Generally at Kīlauea, SO_2 is emitted from specific, well-established vents, while CO_2 degassing is more diffuse and flows through a multitude of fumaroles, fractures, and steaming ground throughout the volcano (Gerlach et al., 2002; Hager et al., 2008). Measuring CO_2 emissions at Kīlauea is important because variations in the emission rate can provide a window into understanding eruption precursors and potentially forecasting volcanic eruptions (Hager et al., 2008). For example, between 2003 and 2007, the magma supply rate to Kīlauea increased drastically (Poland et al., 2012). Indicators of this increase in the magma supply included higher gas emissions, seismicity, deformation, and eruptive activity, but the CO_2 emissions doubled about a year before the other signs appeared (Poland et al., 2012, 2014). This points to the importance of monitoring CO_2 emissions and further exploring their potential for forecasting volcanic eruptions.

The primary method used for measuring the CO_2 flux at Kīlauea before the 2008 summit lava lake was by using the CO_2/SO_2 ratio from the plume and COSPEC measurements of the SO_2 emission rate to calculate the flux (Hager et al., 2008). The southern stretch of Crater Rim Drive has been used since 1979 for correlation spectrometry (COSPEC) due to the north easterly trade winds carrying the summit gas plume across the road at that location (Gerlach et al., 2002). This COSPEC traverse is used to constrain Kīlauea's SO_2 emissions. Additionally, the plume contains high concentrations of CO_2 and SO_2, which allows for the calculation of the summit CO_2/SO_2 ratio (Gerlach et al., 2002).

Equation 4.1: $E_{CO2} = 0.69(CO_2/SO_2)E_{SO2}$

Equation 4.1 is used to calculate the CO_2 emission rate (E_{CO2}) based on the average molar concentration ratio of CO_2 to SO_2 in the summit plume (CO_2/SO_2), the summit SO_2 emission rate (E_{SO2}), and the ratio of the molecular weight of CO_2 to SO_2 which is 0.69.

The first estimates of CO_2 emission rates from the Kīlauea summit caldera occurred in the early 1980s using this method while the East rift zone was experiencing an eruption. Two measurements, taken about a month apart, measured emissions from the Pu‘u ‘Ō‘ō vent at a rate of 4700 tons CO_2/day and 3200 tons CO_2/day (Greenland et al., 1985). The summit caldera was not erupting at this time and emitting approximately 1600 tons CO_2/day (Greenland et al., 1985). Additional measurements have been made since the 1980s further refining and constraining Kīlauea’s CO_2 emissions. In the late 1990s, the emission rate for the summit caldera was measured at 8500 tons CO_2/day and 4900 tons CO_2/day in the early 2000s (Gerlach et al., 2002; Hager et al., 2008). In 2003, a period of summit inflation began at Kīlauea that resulted in an associated CO_2 emission rate increase to an average of ~20,000 tons/day (Poland et al., 2012).

However, in March of 2008 a new eruption began at Kīlauea’s summit that caused a long-term lava lake in the Halema‘uma‘u crater (Patrick et al., 2013; Edmonds et al., 2013). Because of this lava lake, SO_2 degassing concentrated to a single plume rising from the lava lake and the more diffuse SO_2 degassing ceased. The diffuse degassing of CO_2 continued but the lava lake plume was found to be depleted in CO_2 (Edmonds et al., 2013). Because the CO_2 and SO_2 are no longer degassing from the same area, the indirect method of measuring the CO_2 emission rate is no longer accurate and other methods need to be explored in order to determine the CO_2 emission rate.

Over the summer of 2021, a survey of the CO_2 concentrations across the entire caldera was carried out. One of the goals of this project was to construct a comprehensive map of Kīlauea's CO_2 concentrations throughout the entire caldera. A drone mounted with a multiGAS would be used to map the areas of the caldera inaccessible by foot. Additionally, the measurements from 2021 were compared to similar, but smaller-scale, surveys completed in 2001-2002 and 2014 in order to understand whether CO_2 degassing pathways have changed over the past two decades. Finally, potential methods for determining CO_2 flux from the caldera in the future will be discussed and their associated difficulties and challenges.

4.2 Methods

4.2.1 CO_2 emission in the caldera

Gas emissions of CO_2, SO_2, and H_2S from the Kīlauea caldera were measured using two MultiGAS instruments mounted on backpack frames (Figure 4.3). The inlet to the instrument was located at approximately waist height and air was pumped in, analyzed for the gas concentration, and then real-time data was transmitted to hand held devices. This information allowed immediate identification of areas with high CO_2 concentration where more concentrated MultiGAS measurements could be made. A filter was secured over the inlet point in order to prevent dust or ash from getting pulled into the instrument and clogging the tubing.

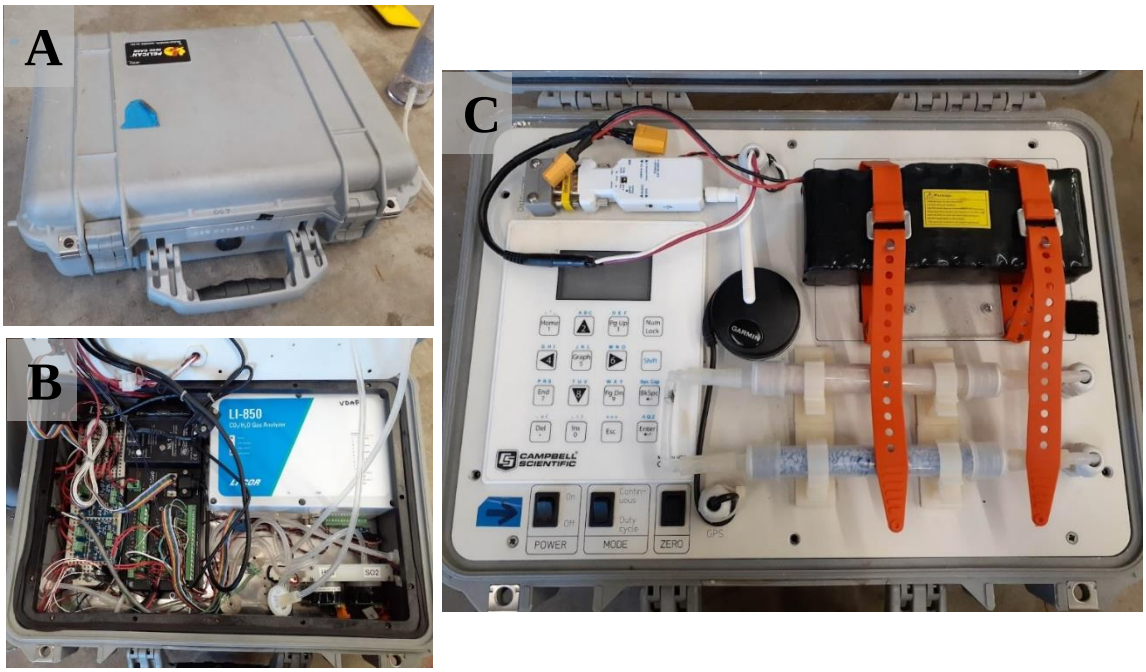

Figure 4.3: A) Outer, hard shell casing for MultiGAS, B) Interior of MultiGAS showing the Li-COR LI-850 CO_2/H_2O analyzer and the City Technology, Ltd. T3ST/F SO_2 sensor and the City Technology, Ltd. T3H H_2S sensor, C) MultiGAS control panel, battery, and GPS.

The MultiGAS used a Li-COR LI-850 CO_2/H_2O analyzer to measure the CO_2 concentrations and a City Technology, Ltd. T3ST/F and T3H to measure the SO_2 and H_2S concentrations, respectively. Prior to each day in the field, the MultiGAS was calibrated using gas cylinders with a known concentration of CO_2, SO_2, and H_2S. A smaller MultiGAS designed to fit on a UAS was also utilized on a few of the days in order to cover ground more efficiently. These sensors saturated at CO_2 concentrations above 5000 ppm, so measurements above this threshold were recorded as 5000 ppm.

The caldera was split into four primary sections (F1, F2, F3, and the down-dropped block [DDB]) plus a large loop around the caldera rim (Figure 4.4). Smooth and relatively easy to traverse terrain in sections F1, F2, and F3 allowed them to be covered by walking straight transects spaced approximately 25-50 m apart with the MultiGAS instruments. However, the terrain in the DDB was highly broken up and hazardous to navigate, resulting

in much more scattered data collection and gaps in the final CO_2 map from areas that were impossible to safely traverse. Additionally, the DDB was only accessible via helicopter, so there was limited time available for mapping that area. In difficult to traverse or time-limited locations, priority was given to vents that were visibly emitting gas or areas with altered rock that indicated elevated gas emissions. In total, 19 days were spent in the field mapping the CO_2 emissions and three of those days were spent mapping the DDB.

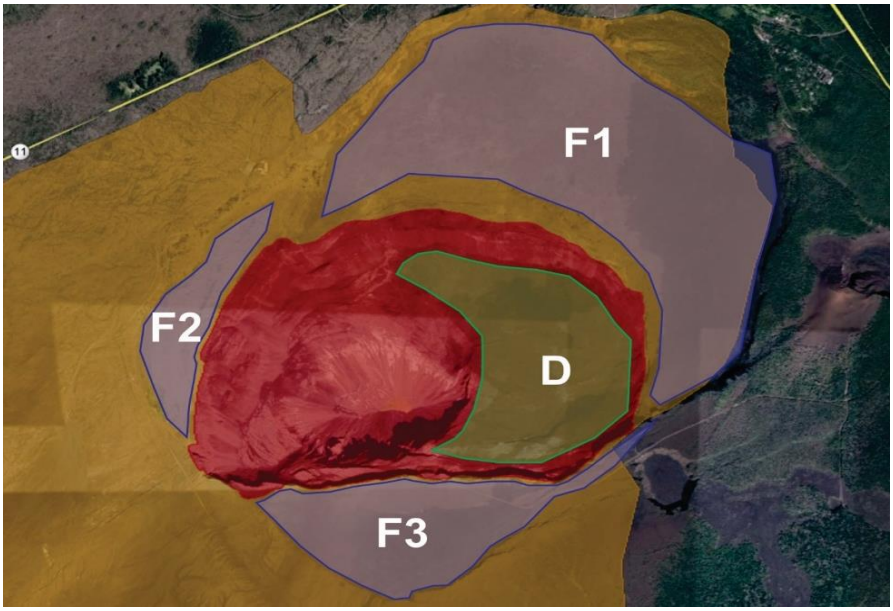

Figure 8.4: Primary sections mapped in and around the Kīlauea caldera. F1 is the caldera floor, F2 and F3 are areas on the rim of the caldera, and D is the down-dropped block. Red indicates areas that were impossible to traverse on foot.

4.2.2 Correction and kriging of CO_2 data

The calibrations of the MultiGAS instruments completed at the beginning of each day were used to correct the raw data. This ensured that potential differences between instruments and gradual drift of measurements over time were accounted for and everything was adjusted to the same base line. Additionally, any data collected outside of the caldera

traverses (i.e., during instrument calibrations, transit to the field site, and extended breaks during the day) was removed from the final dataset in order to avoid skewing the data.

ArcMap 10.8.1 was used to interpolate the corrected data and generate maps of CO_2 concentrations for the entire caldera. Kriging is an interpolation method that accounts for the fact that close together data is likely going to be more similar than data that is farther apart (Shi, 2014). The ArcGIS Geostatistical Wizard tool was used to perform the simple kriging on the data. A normal score transformation was used in order to ensure that the data had a gaussian distribution. A semivariogram was generated for each dataset and used to create the final map of the kriged CO_2 concentration data.

4.3 Results

After corrections, the CO_2 concentration data ranged from 252-4761 ppm. Before these corrections, there were several locations where the CO_2 sensor reached 5000 ppm. At this concentration, the MultiGAS CO_2 sensor saturated, so it is likely that the areas with the highest readings were actually higher than 5000 ppm. In the raw data, most of the elevated CO_2 spots occurred in the southern half of the DDB in a roughly E-W orientation (Figure 4.5). The F1 block also contained an area with highly elevated CO_2 emissions. This area was located on the edge of F1 where the lava flows become extremely broken up before dropping off into the DDB. The only other area with elevated CO_2 emissions occurred at several known CO_2 emitting vents in the Steam Vents area of Hawaii Volcanoes National Park, located towards the top of the map (Figure 4.5).

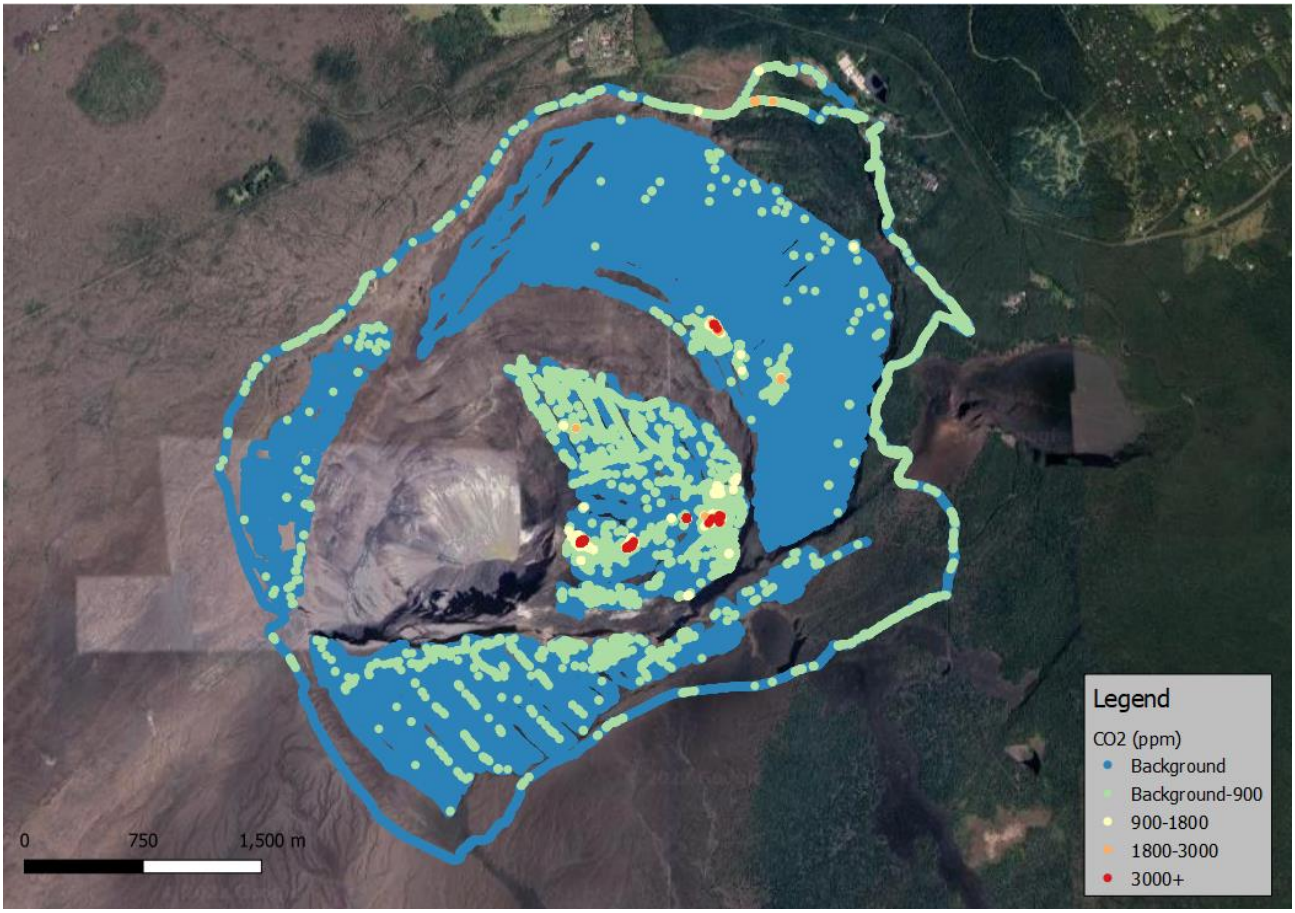

Figure 4.9: Raw CO_2 concentration data from 2021 CO_2 survey. CO_2 concentration is displayed in ppm.

Figure 4.6 shows the CO_2 emissions after the data had been run through simple kriging in ArcGIS. The areas with the highest CO_2 emissions generally correspond to the same locations depicted in Figure 4.5. Blocks F1, F2, and F3 generally show lower CO_2 emissions than the down dropped block. Additionally, the large area of elevated CO_2 emissions towards the top of the map corresponds to the Steam Vents area in Hawaii Volcanoes National Park, which has multiple vents emitting large quantities of CO_2.

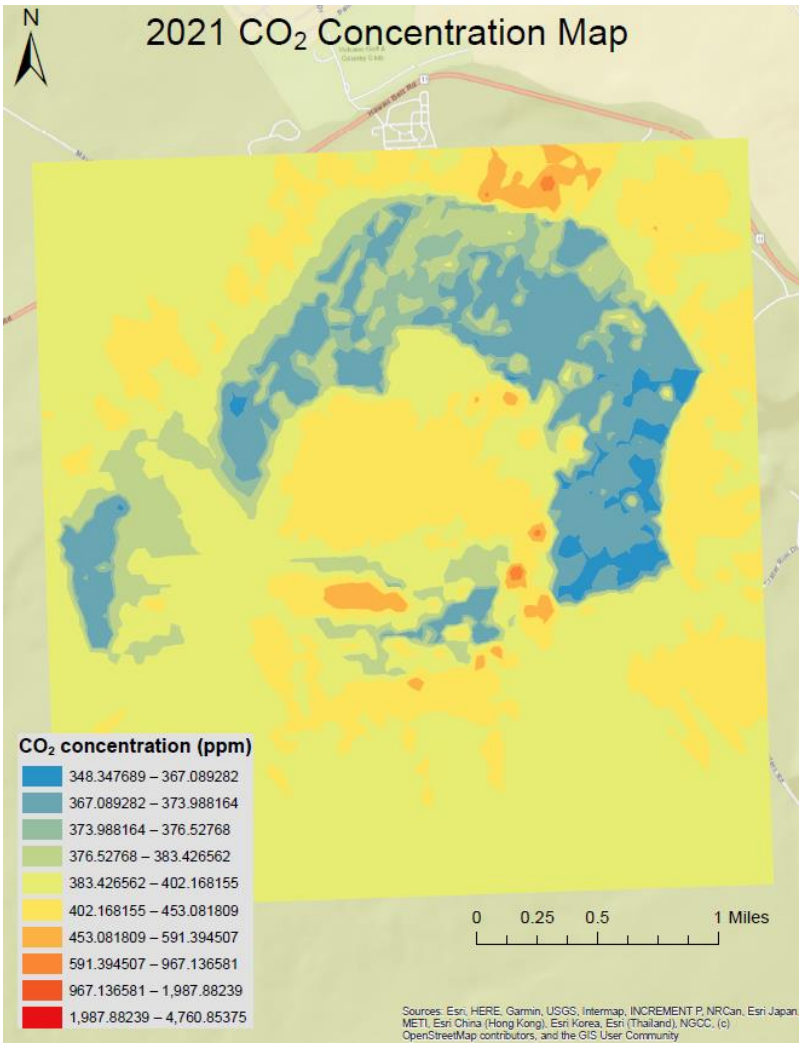

Figure 4.10: Map of kriged CO_2 concentration data from 2021 for the entire caldera

The raw data from the DDB was plotted and kriged separately from the rest of the data in order to display a more detailed map of the highest CO_2 emitting area in the caldera (Figure 4.7). Previous CO_2 surveys covering smaller portions of the DDB identified that most of the visibly steaming and high CO_2 emitting vents were located towards the southern end, so this is where the majority of the mapping in 2021 focused. According to this map, the highest CO_2 emitting area was located along the southwestern edge of the DDB, where it drops into the Halemaʻumaʻu pit crater. Another area with elevated CO_2 concentration was along the southeastern edge where there was a large field of visibly steaming vents.

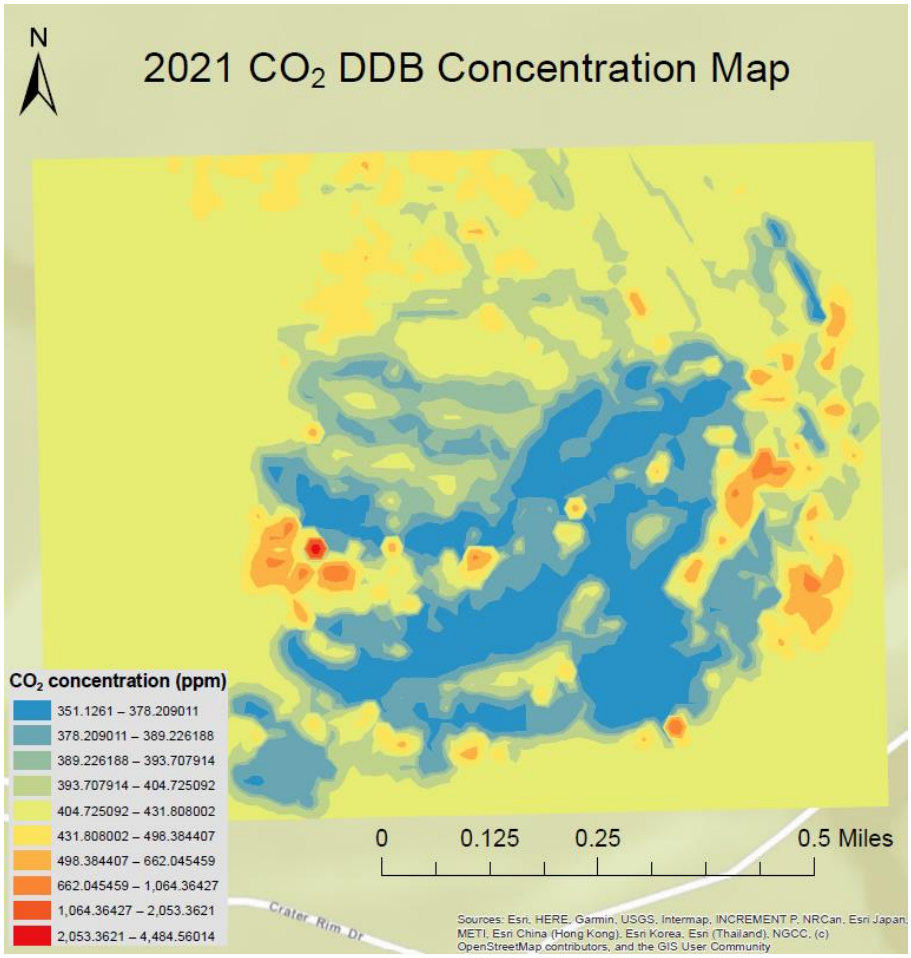

Figure 4.11: Map of kriged CO_2 concentration data from 2021 for the down dropped block.

4.4 Discussion

4.4.1 CO_2 survey comparison

There have been previous CO_2 surveys of smaller areas of the caldera, focusing on the southern part of the now DDB (Figure 4.8). However, when these surveys occurred (2001-2002 and 2014) the caldera floor had not yet collapsed due to the 2018 eruption. All three of the CO_2 surveys (2001-2002, 2014, 2021) have an area in the present-day DDB that overlaps, which can be examined to determine whether CO_2 degassing pathways have

changed through time or shifted because of the caldera collapse in 2018. Figure 4.9 compares the overlapping portion of the survey for each map.

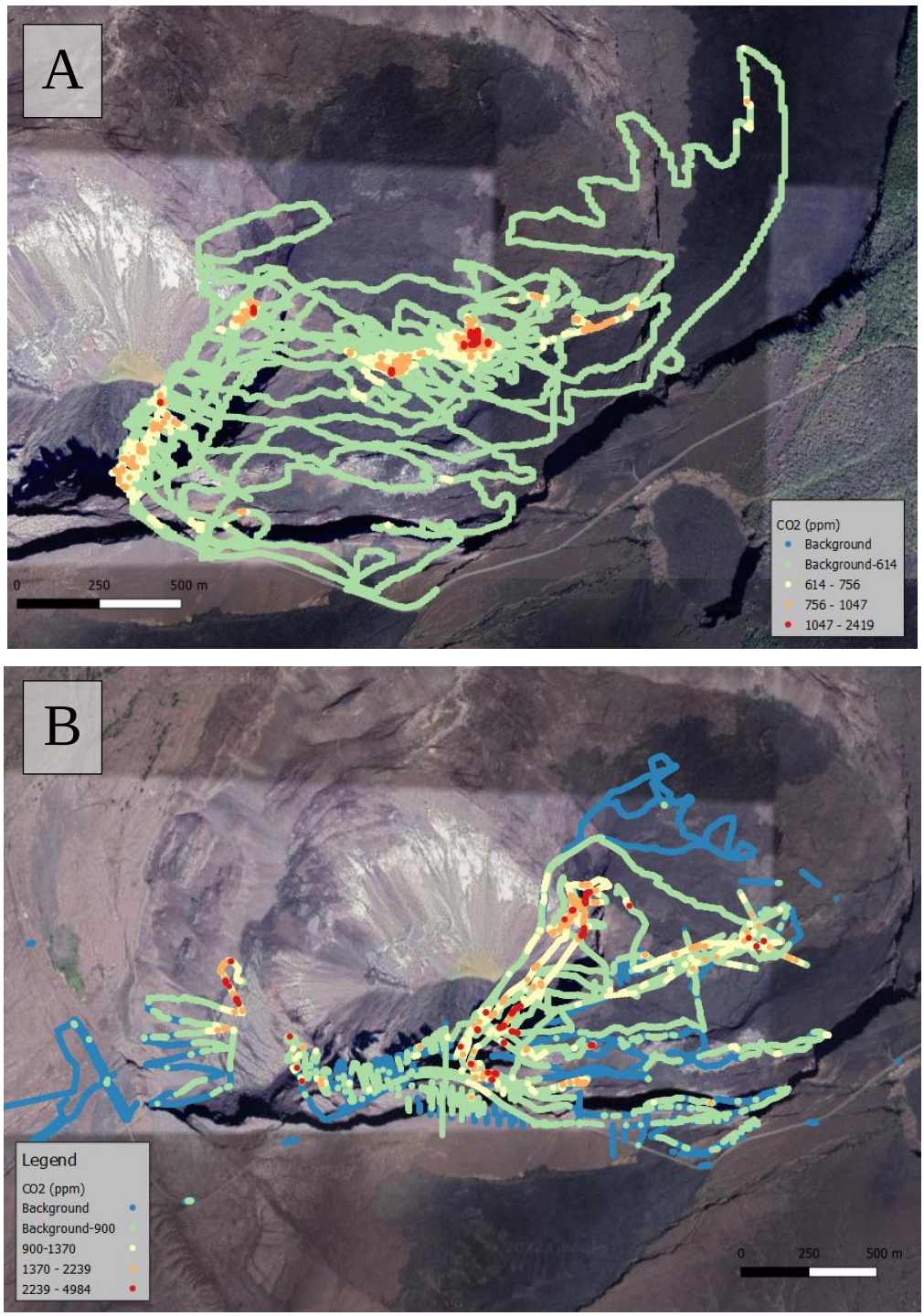

Figure 4.12: A) Raw CO_2 concentration data from 2014, B) Raw CO_2 concentration data from 2001-2002.

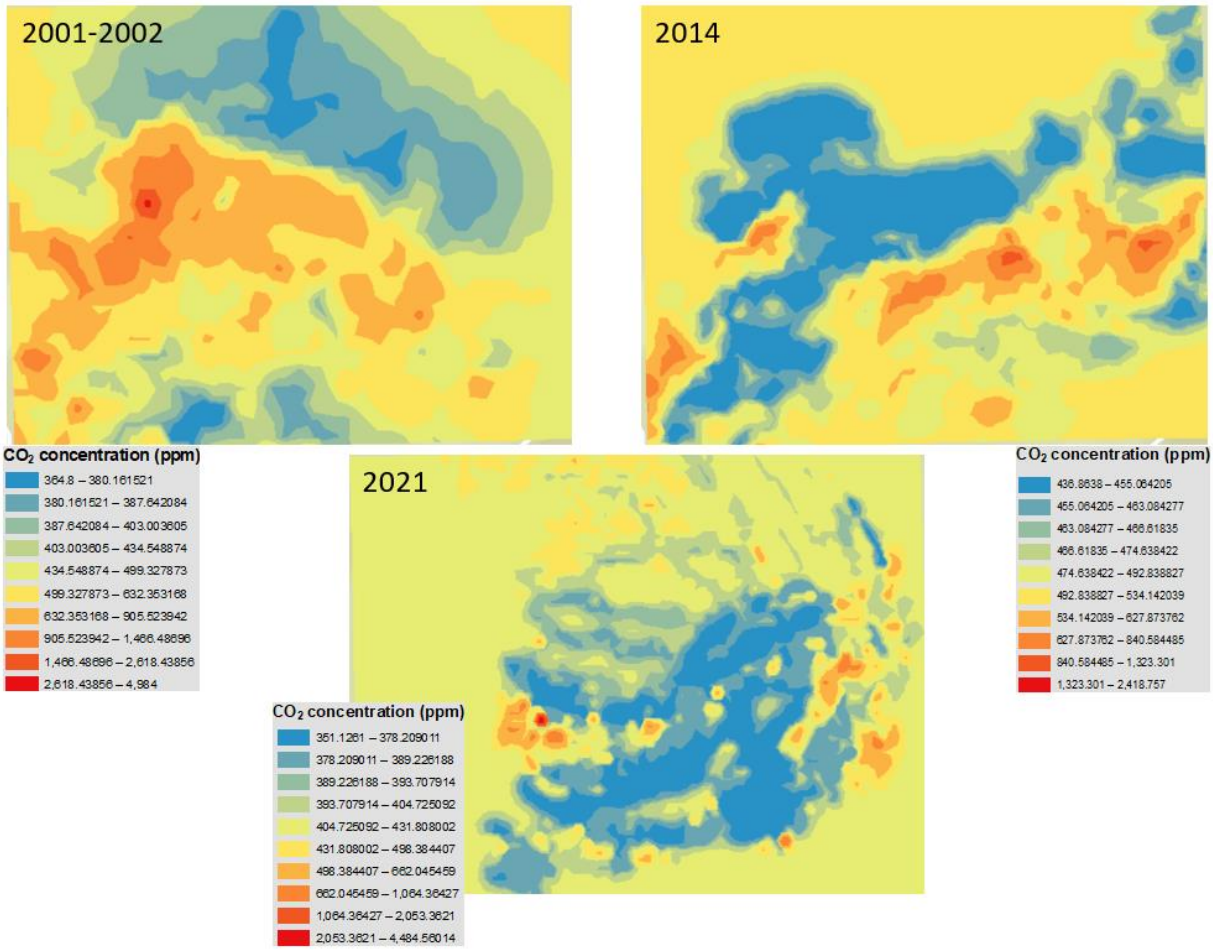

Figure 4.13: Kriged CO_2 concentration maps for surveys conducted in 2001-2002, 2014, and 2021.

From Figure 4.9, it appears that the primary CO_2 hotspots do shift slightly throughout time. During 2001-2002, the highest CO_2 concentrations are located towards the western edge of the map but this shifts more towards the center and eastern edge of the map in 2014. The data from 2021 is more comprehensive and shows the highest concentrations of CO_2 occur along both the western and eastern edges of the map. Something that remains consistent throughout the 3 maps is the high CO_2 measurements tend to concentrate along an E-W line through the center of the map. While the locations of highest CO_2 emissions do shift around slightly, they generally stay in the same area, so it does not appear that the past

20 years and the 2018 eruption and collapse impacted the CO_2 degassing pathways between the magma reservoir and the surface.

Kīlauea's summit has two magma reservoirs, the main South Caldera reservoir and the shallower Halemaʻumaʻu reservoir, that supply magma and gas to the surface (Cervelli and Miklius, 2002; Poland et al., 2014; Carey et al., 2015; Pietruszka et al., 2015). The Halemaʻumaʻu reservoir is located slightly to the east-northeast of the Halemaʻumaʻu crater at a depth of 1-2 km (Poland et al., 2014). Visually, this appears to coincide with the highest CO_2 emissions measured in the DDB. This indicates that the source of the CO_2 degassing is likely the shallow reservoir beneath the main caldera center.

4.4.2 Potential methods to determine CO_2 emissions

Because of the 2008 summit lava lake which concentrated the SO_2 emissions to a single plume while CO_2 emissions remained generally diffuse, the indirect method for determining the CO_2 emission rate using the SO_2 emission rate and the CO_2/SO_2 ratio is no longer feasible or accurate. So, new methods for measuring the CO_2 emission rate need to be investigated. One potential method involves using UAVs to directly measure the CO_2 concentration in a plume and then relate that to the plume speed to calculate the CO_2 flux. Another possible method is to compare a CO_2 flux map created using the soil accumulation chamber method to multiGAS measurements and correlate the data.

When SO_2 is not present in a plume, the only way to measure CO_2 emissions is through direct measurements (Werner et al., 2019). These direct measurements use an airborne vehicle, such as UAVs, downwind from the plume source to measure a vertical

profile of CO_2 concentration. The emission rate of CO_2 can then be determined by multiplying the plume speed by the CO_2 concentration (Werner et al., 2019). This method requires CO_2 concentrations approximately 2-5 ppm above background and uncertainties in plume speed can affect the measurements (Werner et al., 2019).

A common way to determine CO_2 flux is the soil accumulation chamber method which measures the CO_2 accumulating in a chamber of known volume during a known time period (Chiodini et al., 1998). For this method to be successful the ground needs to be soft enough to allow a seal between the chamber and the ground, so that gas cannot escape the chamber and outside air cannot enter the chamber. The Kīlauea caldera is almost entirely made of old lava flows which would not allow the chamber to be pressed into the ground to form this seal. However, the CO_2 flux has been determined using this method at the nearby Puhimau crater. Additionally, a CO_2 concentration survey using a MultiGAS could be carried out at the Puhimau crater. If the two maps have a similar pattern, then a scaling factor could be determined that would relate the soil accumulation chamber survey to the MultiGAS survey. This scaling could then be applied to the map of CO_2 concentrations across the entire caldera collected in 2021 in order to potentially determine a total emission rate of CO_2 from the Kīlauea caldera.

These are two possible methods for determining Kīlauea's CO_2 emission rate. Both require testing in order to determine the accuracy and possible uncertainties associated with each method. One challenge related to using UAVs to determine the CO_2 flux is that Kīlauea does not have a single plume of CO_2 and instead most of the CO_2 is emitted through diffuse degassing. Because of this, it is uncertain whether UAV's will provide a viable method for

measuring the CO_2 being emitted from Kīlauea. For the second method, the plausibility of producing a reliable scaling factor between CO_2 concentration and flux is unknown and requires testing. Both of these methods are good potential directions for researching how to determine Kīlauea's CO_2 emission rate.

4.5 Conclusions

Monitoring volatile emissions from volcanos provides a way to understand subsurface magma movement and potentially forecast eruptions. CO_2 is an especially important volcanic gas and sudden changes in CO_2 emissions can indicate changing conditions at a volcano, possibly leading to an eruption. Kīlauea is one of the most active volcanos in the world, so measuring and monitoring the CO_2 emissions is of extreme importance for understanding Kīlauea's activity. Measuring the total flux of CO_2 is challenging because of the diffuse nature of the CO_2 emissions since the appearance of the 2008 summit lava lake. Creating a comprehensive map of CO_2 concentrations across the caldera and surrounding rim was a first step towards determining the best way to measure CO_2 emissions at Kīlauea.

UAVs are one potential research direction for measuring CO_2 emissions as they can be flown through the gas plume and directly measure the CO_2 and wind speed in order to calculate the flux. Another possible research direction involves correlating CO_2 concentration measurements to CO_2 flux measurements at a nearby caldera and then applying this scaling factor to the CO_2 concentration map produced for the Kīlauea caldera. Both of these approaches have associated difficulties and their plausibility at Kīlauea needs to be tested.

But determining a reliable way to measure the total CO_2 flux from this caldera is vital to understanding and predicting future volcanic activity at Kīlauea.

Acknowledgements

This work was supported by the Additional Supplemental Appropriations for Disaster Relief Act of 2019 (P.L. 116-120) following the eruption of Kīlauea Volcano in 2018. Special thanks to Tricia Nadeau, Tamar Elias, Miki Warren, and Katie Mulliken at the Hawaiian Volcano Observatory for assistance with learning the equipment, working in the field, and analyzing the data.

References

Almendros, J., Chouet, B., Dawson, P., and Bond, T., 2002, Identifying elements of the plumbing system beneath Kīlauea Volcano, Hawaii, from the source locations of very-long-period signals: Geophysical Journal International, v. 148, p. 303–312, doi:10.1046/j.1365-246X.2002.01629.x.

Baker, S., and Amelung, F., 2012, Top-down inflation and deflation at the summit of Kīlauea Volcano, Hawai‘i observed with InSAR: Journal of Geophysical Research: Solid Earth, v. 117, doi:10.1029/2011JB009123.

Battaglia, J., Got, J.-L., and Okubo, P., 2003, Location of long-period events below Kīlauea Volcano using seismic amplitudes and accurate relative relocation: Journal of Geophysical Research: Solid Earth, v. 108, doi:10.1029/2003JB002517.

Carey, R., Cayol, V., Poland, M., Weis, D., Cayol, V., and Cayol, V., 2015, Hawaiian Volcanoes: From Source to Surface: Washington, UNITED STATES, American Geophysical Union, http://ebookcentral.proquest.com/lib/unm/detail.action?docID=1895691 (accessed April 2022).

Cervelli, P.F., and Miklius, A., 2002, The Shallow Magmatic System of Kïlauea Volcano: , p. 16.

Chiodini, G., Cioni, R., Guidi, M., Raco, B., and Marini, L., 1998, Soil CO2 flux measurements in volcanic and geothermal areas: Applied Geochemistry, v. 13, p. 543–552, doi:10.1016/S0883-2927(97)00076-0.

Eaton, J.P., and Murata, K.J., 1960, How Volcanoes Grow: Science, doi:10.1126/science.132.3432.925.

Edmonds, M. et al., 2013, Magma storage, transport and degassing during the 2008–10 summit eruption at Kīlauea Volcano, Hawai‘i: Geochimica et Cosmochimica Acta, v. 123, p. 284–301, doi:10.1016/j.gca.2013.05.038.

Fiske, R.S., and Kinoshita, W.T., 1969, Inflation of Kīlauea Volcano Prior to Its 1967-1968 Eruption: Science, v. 165, p. 341–349.

Gansecki, C., Lee, R.L., Shea, T., Lundblad, S.P., Hon, K., and Parcheta, C., 2019, The tangled tale of Kīlauea’s 2018 eruption as told by geochemical monitoring: Science, v. 366, p. eaaz0147, doi:10.1126/science.aaz0147.

Gerlach, T.M., 1986, Exsolution of H2O, CO2, and S during eruptive episodes at Kīlauea Volcano, Hawaii: Journal of Geophysical Research: Solid Earth, v. 91, p. 12177–12185, doi:10.1029/JB091iB12p12177.

Gerlach, T.M., and Graeber, E.J., 1985, Volatile budget of Kīlauea volcano: Nature, v. 313, p. 273–277, doi:10.1038/313273a0.

Gerlach, T.M., McGee, K.A., Elias, T., Sutton, A.J., and Doukas, M.P., 2002, Carbon dioxide emission rate of Kīlauea Volcano: Implications for primary magma and the summit reservoir: Journal of Geophysical Research: Solid Earth, v. 107, p. ECV 3-1-ECV 3-15, doi:10.1029/2001JB000407.

Greenland, L.P., Rose, W.I., and Stokes, J.B., 1985, An estimate of gas emissions and magmatic gas content from Kīlauea volcano: Geochimica et Cosmochimica Acta, v. 49, p. 125–129.

Hager, S.A., Gerlach, T.M., and Wallace, P.J., 2008, Summit CO2 emission rates by the CO2/SO2 ratio method at Kīlauea Volcano, Hawai‘i, during a period of sustained inflation: Journal of Volcanology and Geothermal Research, v. 177, p. 875–882, doi:10.1016/j.jvolgeores.2008.06.033.

Johnson, D.J., Eggers, A.A., Bagnardi, M., Battaglia, M., Poland, M.P., and Miklius, A., 2010, Shallow magma accumulation at Kīlauea Volcano, Hawai‘i, revealed by microgravity surveys: Geology, v. 38, p. 1139–1142, doi:10.1130/G31323.1.

Kern, C., Lerner, A.H., Elias, T., Nadeau, P.A., Holland, L., Kelly, P.J., Werner, C.A., Clor, L.E., and Cappos, M., 2020, Quantifying gas emissions associated with the 2018 rift eruption of Kīlauea Volcano using ground-based DOAS measurements: Bulletin of Volcanology, v. 82, p. 55, doi:10.1007/s00445-020-01390-8.

Patrick, M.R., Dietterich, H.R., Lyons, J.J., Diefenbach, A.K., Parcheta, C., Anderson, K.R., Namiki, A., Sumita, I., Shiro, B., and Kauahikaua, J.P., 2019, Cyclic lava effusion during the 2018 eruption of Kīlauea Volcano: Science, v. 366, p. eaay9070, doi:10.1126/science.aay9070.

Patrick, M., Orr, T., Sutton, J., Elias, T., and Swanson, D., 2013, The First Five Years of Kīlauea’s Summit Eruption in Halema‘uma‘u Crater, 2008-2013: USGS Fact Sheet Fact Sheet.

Pietruszka, A.J., and Garcia, M.O., 1999, The size and shape of Kīlauea Volcano’s summit magma storage reservoir: a geochemical probe: Earth and Planetary Science Letters, v. 167, p. 311–320, doi:10.1016/S0012-821X(99)00036-9.

Pietruszka, A.J., Heaton, D.E., Marske, J.P., and Garcia, M.O., 2015, Two magma bodies beneath the summit of Kīlauea Volcano unveiled by isotopically distinct melt

deliveries from the mantle: Earth and Planetary Science Letters, Volume 413, p. 90-100., v. 413, p. 90, doi:10.1016/j.epsl.2014.12.040.

Poland, M.P., Miklius, A., Sutton, A.J., and Thornber, C.R., 2012, A mantle-driven surge in magma supply to Kīlauea Volcano during 2003-2007: Nature Geoscience, v. 5, p. 295300, doi:10.1038/ngeo1426.

Poland, M.P., Takahashi, T.J., and Landowski, C.M., 2014, Characteristics of Hawaiian volcanoes: U.S. Geological Survey professional paper: 1801.

Shi, G., 2014, Chapter 8 - Kriging, *in* Shi, G. ed., Data Mining and Knowledge Discovery for Geoscientists, Oxford, Elsevier, p. 238–274, doi:10.1016/B978-0-12-410437-2.00008-4.

Tilling, R.I., and Dvorak, J.J., 1993, Anatomy of a basaltic volcano: Nature, v. 363, p. 125–133, doi:10.1038/363125a0.

Werner, C. et al., 2019, Carbon Dioxide Emissions from Subaerial Volcanic Regions: Two Decades in Review, *in* Orcutt, B.N., Daniel, I., and Dasgupta, R. eds., Deep Carbon: Past to Present, Cambridge, Cambridge University Press, p. 188–236, https://www.cambridge.org/core/books/deep-carbon/carbon-dioxide-emissions-from-subaerial-volcanic-regions/F8B4EFAE0DAF5306A8D397C23BF3F0D7 (accessed July 2022).

Wright, T.L., and Klein, F.W., 2014, Two hundred years of magma transport and storage at Kīlauea Volcano, Hawai'i, 1790-2008: U.S. Geological Survey Professional Paper USGS Numbered Series 1806, 258 p., doi:10.3133/pp1806.